Time-Resolved Characterization of Carrier and Phonon Dynamics in GaN Single Crystals

by

Shuai Wu

Submitted in Partial Fulfillment
of the
Requirements for the Degree
Doctor of Philosophy

Supervised by

Professor Roman Sobolewski

Department of Physics and Astronomy
The College
Arts & Sciences

University of Rochester
Rochester, New York

2007

Curriculum Vitae

The author was born in Huaibei Anhui, China on August 22, 1976. He attended the University of Science and Technology of China from 1993 to 2000, and graduated with a Bachelor of Science degree in 1997 and a Master of Science degree in 2000. He came to the University of Rochester in the Fall of 2000 and began graduate studies in the Department of Physics and Astronomy. He has received a Frank Horton Graduate Fellowship from the laboratory for laser energetics from 2000 to 2007. He pursued his research in the Ultrafast Quantum Phenomena Laboratory under the direction of Professor Roman Sobolewski and received the Master of Arts degree from the University of Rochester in 2002.

Acknowledgements

I have been very fortunate to have the privilege of working with Professor Roman Sobolewski, which turned out to be an exciting and rewarding learning experience. It is his sharp insight, enlightened guidance, and generous support that made it possible for me to finish a project like this. He also took a genuine interest in my personal development and ensured my growth by constant demands, advice and encouragement. I deeply appreciate the best of opportunities Professor Sobolewski provided me, and credit his belief in my capabilities as an inspiration for achievement of my academic career.

I would like to thank all the members (both past and present) in the ultrafast optoelectronics research community at the Laboratory for Laser Energetics. Along with other members of the Department of Physics and Astronomy, they have made my graduate study fruitful. From such a long list, I am particularly thankful to Dr. Xuemei Zheng for her patience and willingness to help me overcome many problems and frustrations I experienced in my experiments early years. I would also appreciate the friendship and help in various manners from Dr. Jung-Rae Park, Marat Khafizov, Daozhi Wang, Allen Cross, Xia Li, Jennifer Kitaygorsky, Dong Pan, Jie Zhang, and Takahiro Taneda.

My graduate experience has been enhanced through the collaboration with the Solid State Physics Laboratory at ETH, Zurich, Switzerland and the Institute of Thin Films and Interfaces, Research Center Jülich, Germany. I am grateful to Professor

Janusz Karpinski and Dr. Martin Mikulics for providing me very high-quality samples.

I am also thankful for the financial support from the Frank Horton Graduate Fellowship Program at the Laboratory for Laser Energetics of the University of Rochester.

I would also like to express my gratitude to my family for their support and patience throughout many years of my school study. Finally, but most heartily, I would thank my wife, Zhuoyan Ou, for her deep love, understanding, support, and tolerance.

Abstract

This thesis presents a comprehensive study of time-resolved intervalley transitions of hot electrons, as well as generation and detection of coherent acoustic phonons, in high-quality GaN single crystals, using a two-color (ultraviolet and near-infrared), femtosecond, pump–probe spectroscopy technique.

In investigation of the intervalley transitions of electrons between the conduction Γ band and the L valley, we have found that the threshold for the $\Gamma \leftrightarrow L$ transition appears at the energy of 4.51±0.05 eV at room temperature and shifts to 4.57±0.01 eV at 100 K. At both temperatures, the measured electron $\Gamma \rightarrow L$ scattering time is limited by the 170-fs width of our pump pulses, while the return $L \rightarrow \Gamma$ process is measurably slower and equals 1.02 ps. The total depopulation time of the L valley is estimated to be ~20 ps. Our physical model, based on the three-state rate equations, fitted our experimental data very well and allowed us to calculate the optical phonon emission time of 290 fs. The deformation potential between the two valleys was also obtained from the intervalley scattering modeling and the value found to be 0.92×10^9 eV/cm.

We also report on our experimental and theoretical studies of the time-resolved generation and detection of coherent acoustic phonons (CAPs). A train of ultraviolet laser pulses with energy above the GaN energy gap induced a transient electronic stress at the GaN surface, responsible for CAP generation. Subsequent CAP oscillations, propagating without any measurable intrinsic attenuation, were

observed by scanning the transient differential reflectivity signal ($\Delta R/R$) of the near-infrared, far-below-bandgap probe beam. The $\Delta R/R$ CAP oscillation amplitude was of the order of 10^{-5} to 10^{-6} and was dependent only on the pump-photon absorption coefficient spectral characteristics. The CAP oscillation frequency was dispersionless (proportional to the probe-beam wave vector), with the slope corresponding to 8002 ± 22 m/s—the speed of sound in GaN—while the CAP signal phase was constant within the entire range of our experiments. The above experimental results are in excellent agreement with our theoretical modeling and the published literature data.

Table of Contents

List of Tables

List of Figures

Chapter One: Introduction

1.1 Gallium nitride overview and thesis motivation

Since the first transistor was invented by John Bardeen, William Shockley, and Walter Brattain in 1947, semiconductor technology has been the center of the amazing technological revolution we are witnessing in computing, communications, consumer electronics, transportation, health care, and just about every sphere of life. As the most important semiconductor, silicon has had a monumental impact on our society. It is the heart of almost any electronic device. Despite its overwhelming success in modern electronics, silicon shows limitations in high-power, high-frequency, and high-temperature applications, which in many areas are the trend in future semiconductor devices. For example, silicon-based RF power transistors, which form the basis of current power amplifiers, cannot deliver the RF power efficiently at the signal purity levels required for cost- and capacity-effective 3G networks. The rapidly growing semiconductor industry is driving silicon to its theoretical materials limits, simultaneously creating opportunities for the next-generation of semiconductors.

In search of new materials, researchers have focused their attention on the group III-V Ga-based semiconductors and most recently on the nitride-based compounds. The wide-bandgap nature of, e.g., GaN renders it suitable for the

fabrication of electronic devices capable of operating under very high power and elevated temperature conditions, as well as optoelectronic devices operating in the blue and UV spectral regions. As a member of the III-V nitrides, Gallium nitride is by far the most extensively studied and has been recognized as the most promising material for future optoelectronic and high-power electronic applications for its superior physical attributes.

GaN was first synthesized in the form of a powder by Johnson *et al.* [1] in 1928 and has been noted as an exceedingly stable compound. Its chemical and thermal stability, combined with the wide bandgap, have made GaN extraordinarily tolerant of elevated temperatures and caustic environments. However, the same attributes that make GaN an excellent semiconductor also make it extremely difficult to manufacture. High quality GaN thin films had not been realized until 1969, when Maruska and Tietjen used a chemical vapor deposition technique to epitaxially grow a large-area layer of GaN on sapphire [2]. All GaN films fabricated at that time suffered from poor crystalline quality and high n-type background carrier concentrations. Almost two decades later, the first p-type GaN was achieved by Akasaki and Amano [3]. This breakthrough opened the door to the blue light emitters and led to a resurgence of interest in GaN electronics.

Recent years have been fueled by a number of critical advances in the both thin-film and bulk-crystal growth, leading to processing technologies of GaN and, eventually, applications, such as blue/green/ultraviolet LEDs, laser diodes, photodetectors, power amplifiers, *etc.* However, much work remains to be

accomplished, both in the development of GaN device technology, and in the determination of the fundamental physical properties of this material.

1.1.1 Properties of the GaN semiconductor

GaN is a direct and wide bandgap III-V compound with the gap energy $E_g =$ 3.4 eV at room temperature, which enables GaN devices to support internal electric fields about five times higher than Si or GaAs. Higher electric fields result in higher breakdown voltages, a critical attribute for handling high-power requirements and for achieving much higher efficiencies through the use of higher supply voltages.

GaN can crystallize in both the wurtzite and zincblende forms. However, the wurtzite polytype appears to be most extensively studied. Table 1.1 demonstrates the physical properties of wurtzite GaN and other well-known semiconductors.

Table 1.1 Physical properties of wurtzite GaN and other well-known semiconductors.

	GaN	Si	GaAs	AlN	6H-SiC	Diamond
Bandgap (eV) @ 300°C	3.4 direct	1.1 indirect	1.4 direct	6.2 direct	2.9 indirect	5.5 indirect
Dielectric constant (static)	8.9	11.7	12.9	8.5	9.7	5.7
Electron mobility (cm^2/V·s)	1000 (bulk)	1400	8500	135	600	2200
Hole mobility (cm^2/V·s)	30	450	400	14	40	1800
Saturation velocity (10^7 cm/s)	2.5	1	2	1.4	2	2.7
Breakdown field (10^6 V/cm)	>5	0.3	0.4	1.2-1.8	4	10
Thermal conductivity (W/cm·K)	1.5	1.5	0.5	2	5	6-20
Melting temperature (°C)	>1700	1412	1240	3000	>1827	4373

We note that among these semiconductors (except diamond), GaN is characterized by

1) low dielectric constant;

2) high electron mobility considering the magnitude of the bandgap;

3) high saturation velocity;

4) high breakdown field;

5) high thermal conductivity; and

6) high melting temperature.

These properties translate to fundamental performance advances of GaN in the area of high-power, high-frequency operations.

A combined figure-of-merit (CFOM) for evaluating semiconductors for high-frequency, high-power/high-temperature applications can be defined as

$$CFOM = \chi \varepsilon \mu V_s E_b^2, \qquad (1.1)$$

where χ is the thermal conductivity, ε the dielectric constant, μ the electron mobility, V_s the saturation velocity, and E_b the breakdown field strength. Figure 1.1 shows the CFOM for GaN, 6H-SiC, GaAs, and Si, and illustrates that GaN offers much higher performance potential than Si or GaAs.
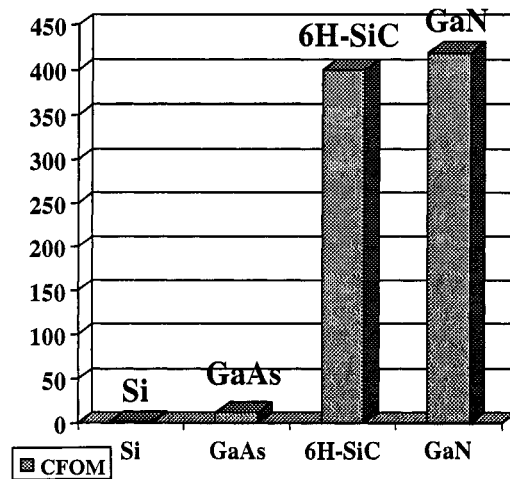
Fig. 1.1 CFOM for Si, GaAs, 6H-SiC, and GaN.

Note that SiC has also a very high CFOM value. However, its indirect bandgap limits applications in optoelectronics. The strongest feature of GaN compared to SiC is the heterostructure technology it can support. Quantum wells, modulation-doped hetero-interfaces, and heterojunction structures can all be made in

GaN-based systems, giving access to new spectral regions for optical devices and new operation regimes for electronic devices.

Other advantageous properties of GaN include high mechanical and thermal stability, the large piezoelectric constant, and novel room-temperature ferromagnetism in Mn-doped GaN.

1.1.2 Applications for GaN semiconductor

There are currently three major applications for GaN-based materials and devices, namely

1.   UV optical sources and photodetectors;

2.   power amplifiers, ultra-high-power switches, and monolithic microwave integrated circuits (MMICs);

3.   room temperature, ferromagnetic semiconductors for spintronics.

GaN-Based UV Optical Sources and Photodetectors

GaN alloyed with AlN and InN spans a wide and continuous range of bandgaps from 1.9 eV to 6.2 eV, e.g., from the visible light well into the ultraviolet wavelengths [4]. This makes the nitride system attractive for optoelectronic device applications, such as light emitting diodes (LEDs), laser diodes (LDs), and detectors, which are active in the green, blue, or UV wavelengths. Particularly, the combination of GaN-based blue and green LEDs with GaAs-based red LEDs forms the basis for large-scale solid-state displays and white light illumination. The solid-state white

light source generated by mixing the primary colors in a light scrambling configuration would not only provide compactness and high lifetime, but also reduce power consumption by 80-90% compared to conventional incandescent or fluorescent light sources.

Digital storage especially benefits from short-wavelength coherent sources based on GaN, because the diffraction limited optical storage density increases roughly quadratically with the reduction of the probe laser wavelength. GaN-based photodetectors are useful for solar-blind UV detection and have applications as biological and chemical agent warning sensors with fast response and high sensitivity.

GaN-Based Power Electronics

The GaN materials system is attractive from the viewpoint of fabricating unipolar power devices, because of its large bandgap and relatively high electron mobility. An example is the use of Schottky diodes as high-voltage rectifiers in power switching applications. These diodes have lower blocking voltages than p-i-n rectifiers, but have advantages in terms of switching speed and the lower forward voltage drop.

GaN-based transistors exhibit a unique combination of high current density, high breakdown electric field, and good thermal conductivity, which enables previously unrealizable microwave power performance for solid state-transistors and MMICs. For microwave power amplification, in satellite links and wireless communication networks, an AlGaN/GaN high-electron-mobility-transistor (HEMT)

has emerged as the most promising device. A typical AlGaN/GaN HEMT shows a sheet carrier density up to ~1.5×10^{13} cm^{-2} (roughly an order of magnitude higher than for GaAs HEMTs), a unity current gain frequency of 65 GHz and a maximum oscillation frequency of 180 GHz. Output powers up to 9.8 W/mm at 8 GHz (power-added efficiency at 47%) have been reported for large periphery GaN HEMTs. It has also been shown that these devices can achieve low microwave added noise figure (NF = 0.6 dB at 10 GHz), while maintaining a large breakdown voltage (>60 V) and, hence, a large dynamic range. Very high voltage (~1 kV) and low frequency (<100 MHz) switching power control are also possible using this device.

GaN for Spintronic Applications

Numerous recent reports have demonstrated room-temperature ferromagnetism in GaN upon Mn doping [5]. Ferromagnetic semiconductors are important materials for spintronics, because of their potential as spin-polarized carrier sources and easy integration with the conventional semiconductor technology. The expected advantages of spin devices include non-volatility, higher integration densities, lower power operation and higher switching speeds. GaN-based ferromagnetic materials are promising for the new generation of device and circuits, including spin transistors, ultra-dense non-volatile semiconductor memory and optical emitters with polarized output.

Because of its increasing importance, studies of the basic properties of GaN crystals, such as carrier and phonon dynamics, the main topics of this thesis, are becoming very pressing.

1.2 Carrier and phonon dynamics in semiconductors

In semiconductors, both carriers and phonons are elementary excitations. "Carriers" mean the conduction-band electrons or valence-band holes. "Phonons" are the quanta of the optical and acoustic modes of lattice vibrations. The nonequilibrium dynamics of carriers and phonons are governed by interactions among these excitations, such as carrier-carrier scattering, carrier-phonon interaction, interaction of carriers with defects or impurities, phonon-phonon scattering, plasma-phonon coupling, and others. Figure 1.2 schematically shows representative processes in semiconductors, taking place within different time scales, ranging from several femtoseconds to several hundred picoseconds. Some of these processes, such as electron-optical-phonon scattering and hole-optical-phonon scattering, have been extensively investigated for GaN before. It was found that longitudinal optical (also called polar optical) phonons play an important role in the electron- (or hole-) phonon scattering processes [6]. Low-energy electrons, near the bottom of the conduction band central valley, because of their s-like wavefunctions, only interact with longitudinal optical phonons through Fröhlich interaction. The matrix elements of the Fröhlich interaction vary inversely with the optical phonon wave vector; thus the

interaction is the most efficient for zone center's polar optical phonons. Holes, which occupy p-like states in the valence band, can interact with phonons through both polar and non-polar coupling. Since the Fröhlich interaction rate varies as $m^{*1/2}$, the heavier holes interact more strongly with the longitudinal optical phonons than the lighter electrons.

Time

$\geq$ 100 ps	• Electron-hole recombination
$\sim$ 1–100 ps	•Carrier-acoustic phonon interaction •Decay of optical phonons
$\leq$ 2 ps	•Electron-optical phonon scattering •Intervalley scattering (Satellite valleys → Central valley)
$\leq$ 200 fs	•Intervalley scattering (Central valley → Satellite valleys) •Hole-optical phonon scattering •Carrier-carrier scattering

0
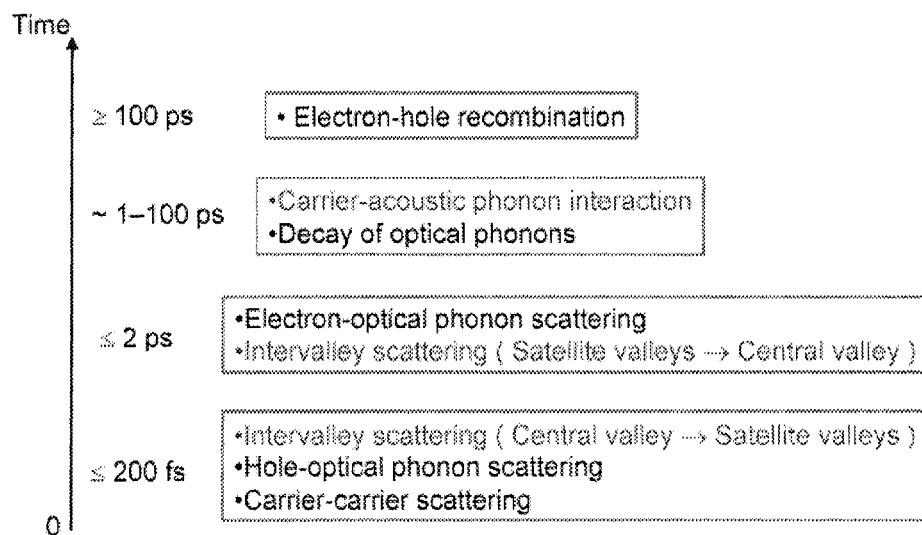
Fig. 1.2 Representative dynamics processes in semiconductors, taking place within different time scales.

High-energy electrons in the conduction band central valley or electrons in the satellite valleys can also interact with large wave vector optical phonons (both longitudinal and transverse modes) through non-polar deformation potential scattering. This interaction is responsible for intervalley transitions of electrons in GaN and is of fundamental importance in understanding the high-field electronic transport properties of this material.

Interactions between electrons and acoustic phonons are also important from both basic-research and technological points of view. For small wave vectors near the center of the Brillouin zone, acoustic phonons have low energies and are not very efficient for cooling of electrons. However, excited electrons can break the lattice equilibrium, resulting in a strong deformation potential-coupled electronic stress, which is responsible for generation of coherent acoustic phonons (CAPs) in GaN. My studies focus on the physics of intervalley transitions of hot electrons, as well as on generation and propagation of CAPs, both, in very high quality GaN single crystals.

1.3   Outline of the thesis

This thesis is focused on intervalley transitions of hot electrons and generation and detection of CAPs in GaN single crystals, investigated by the femtosecond two-color pump-probe spectroscopy. The remainder of the thesis is arranged in four chapters.

In the first part of Chap. 2, preparation of our GaN single crystals is briefly introduced and the basic optical properties of GaN samples, studied by conducting the transmission and reflection measurements, are presented. The remaining of Chap. 2 provides an overview of the pump-probe spectroscopy and describes our femtosecond UV pump and near-infrared (NIR) probe experimental setup in detail.

In Chap. 3, we first introduce our experimental approach to the direct observation of time-resolved intervalley transitions of electrons between the

conduction Γ band and the L valley in GaN single crystals. Next, our experimental results measured at room temperature and at 100 K are presented and interpreted using the solution of the three-state rate equations, which yield the intervalley scattering times, optical phonon emission time, and the deformation potential between the Γ and L valleys.

Chapter 4 is devoted to CAP oscillations in GaN single crystals. We start our presentation with theoretical modeling, where the generation mechanism of CAPs is predicted and the CAP oscillation amplitude, frequency, phase, and attenuation are discussed. After the model, we report our experimental results and compare them with the theoretical ones.

Finally, Chap. 5 summarizes the accomplishments of the work performed in this thesis and presents some ideas for future investigations.

References:

[1]   W. C. Johnson, J. B. Parsons and M. C. Crew, *J. Phys. Chem.* **36**, 2561 (1932).

[2]   H. P. Maruska and J. J. Tietjen, *Appl. Phys. Lett.* **15**, 367 (1969).

[3]   I. Akasaki, T. Kozowa, K. Hiramatsu, N. Sawak, K. Ikeda and Y. Ishii, *J. Lumin.* **40-41**, 121 (1988).

[4]   S. N. Mohammad, A. Salvador and H. Morkoç, *Proceedings of the IEEE*, **83**, 1306 (1995).

[5]   M. L. Reed, *Appl. Phys. Lett.* **79**, 7473 (2001).

[6]   Doctoral thesis: *Hot carrier dynamics in GaN*, by Hong Ye, the University of Rochester (2000).

Chapter Two: GaN sample preparation and pump-probe experiments

2.1 Sample preparation

Our GaN single crystals were grown at Professor Karpinski's group at the Solid State Physics Laboratory at ETH Zurich, Switzerland, using a high-pressure solution-growth (HPSG) method [1]. Figure 2.1 schematically shows the ETH high-temperature, high-pressure crystal growth apparatus. The growth process was carried out at an external nitrogen gas pressure of 8-14 kbar and temperatures of 1350–1600°C, because of high solubility of GaN in Ga at high temperatures. Nitrogen was first compressed with a commercial compressor up to 3 kbar and then compressed up to 10-15 kbar with a pressure intensifier. The pressure intensifier chamber had an internal diameter of 30 mm and in this chamber the high temperature furnace with a Pt-Rh heater was placed. Nitrogen was then transported into the metallic Ga melt with a temperature gradient of 5-50 °C/cm. GaN single crystals formed at the cooler zone of the HPSG chamber. They grew up to 1-mm-thick platelets with typical sizes of up to $3 \times 4 \, mm^2$, as shown in Fig. 2.2. These crystals exhibited an excellent wurtzite crystalline structure, while their morphology depended on the growth process pressure, temperature range, and nitrogen supersaturation. In all our experiments, we

have studied several ~2.5×2.5 mm², transparent (slightly brownish) GaN crystal

pieces, typically ~0.4-mm thick.
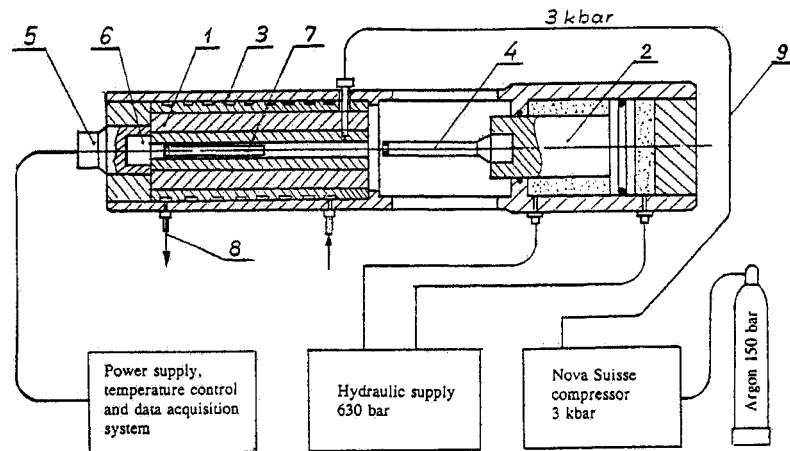
Fig. 2.1 Pressure intensifier and high pressure – high temperature crystal growth chamber for nitrogen pressure up to 15 kbar. 1) 3-mantle high pressure chamber with cooling jacket, 2) press piston, 3) integral body of the intensifier, 4) piston, 5) screw, 6) plug with electrical leads, 7) heater with crucible and sample, 8) cooling system, 9) capillary.
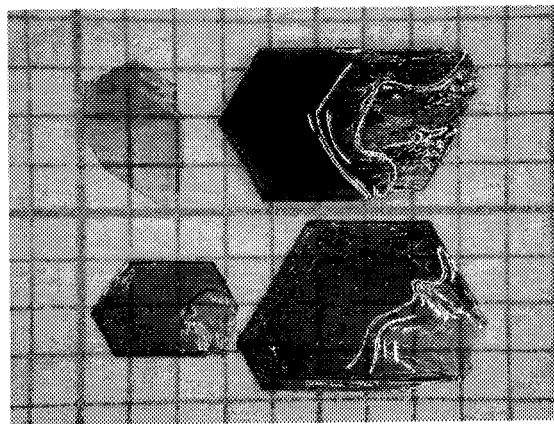
Fig. 2.2 Representative GaN single crystal samples prepared by the HPSG method.

2.2 Optical properties of GaN single crystals

The optical transmission and reflection of our GaN samples were measured at the Laboratory for Laser Energetics, University of Rochester, using a Perkin-Elmer Lambda 900 spectrophotometer at normal incidence by scanning the wavelength from 300 nm to 800 nm. The results are shown in Fig. 2.3. As we can see, the UV to visible contrast is more than 3 decades (at 300 nm the reading is about 0.01%, the limit of the instrument; at 600 nm the reading is about 23%).
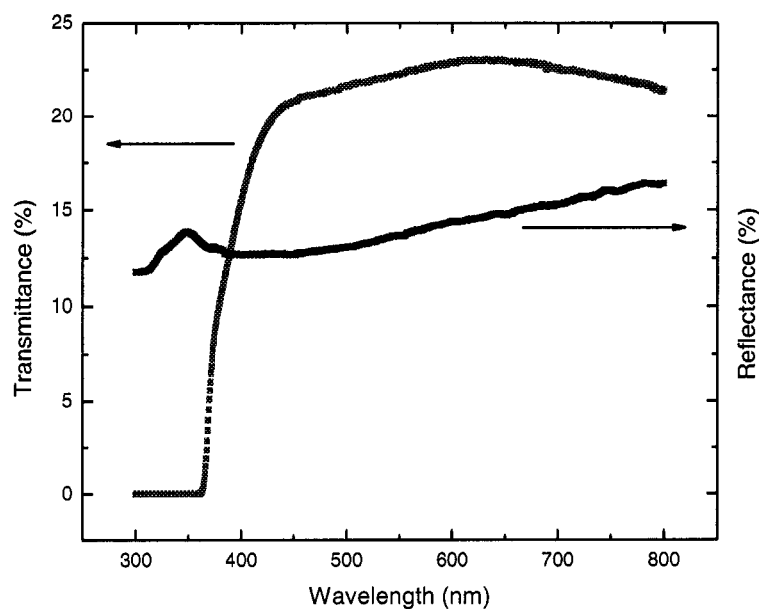
Fig. 2.3. Optical transmittance and reflectance of a GaN single crystal with the area of ~2.5×2.5 mm^2 and thickness of ~ 0.4 mm.

The absorption coefficient spectrum of our GaN single crystal can be extracted from the transmission and reflection data. For the light being incident on a thick sample, its reflection from the rear surface is negligible and the optical transmittance has a rather simple relationship with the optical absorption coefficient, as described by

$$T = (1-R)^2 e^{-\alpha d}, \qquad (2.1)$$

where T is the transmittance, R is the reflectance, α is the absorption coefficient, and d is the sample thickness. From Eq. (2.1), one gets

$$\alpha = \frac{1}{d} \ln \frac{(1-R)^2}{T}. \qquad (2.2)$$

By using Eq. (2.2) with the measured transmission and reflection spectra, the spectral dependence of α can be calculated. Figure 2.4 shows the normalized absorption spectrum of our GaN sample. The sharp absorption edge observed in Fig. 2.4 corresponds to the band-to-band transition and appears at around 3.4 eV (the wavelength: 365 nm). The energy bandgap E_g can be directly determined from the absorption spectrum by using the Tauc relation for a direct-bandgap material [2]:

$$\alpha h v = A(h v - E_g)^{1/2}, \qquad (2.3)$$

where A is a constant and $h\nu$ is the photon energy. To measure E_g from the absorption spectrum, a graph $[(\alpha - \alpha_1)h\nu]^2$ versus $h\nu$ [3] is plotted in Fig. 2.5. We note α_1 is the minimum value of the absorption coefficient. The straight line extrapolation to $[(\alpha - \alpha_1)h\nu]^2 = 0$ gives the value $E_g = 3.387$ eV of our GaN single crystal. This result is in very good agreement with the literature reported values [4,5].
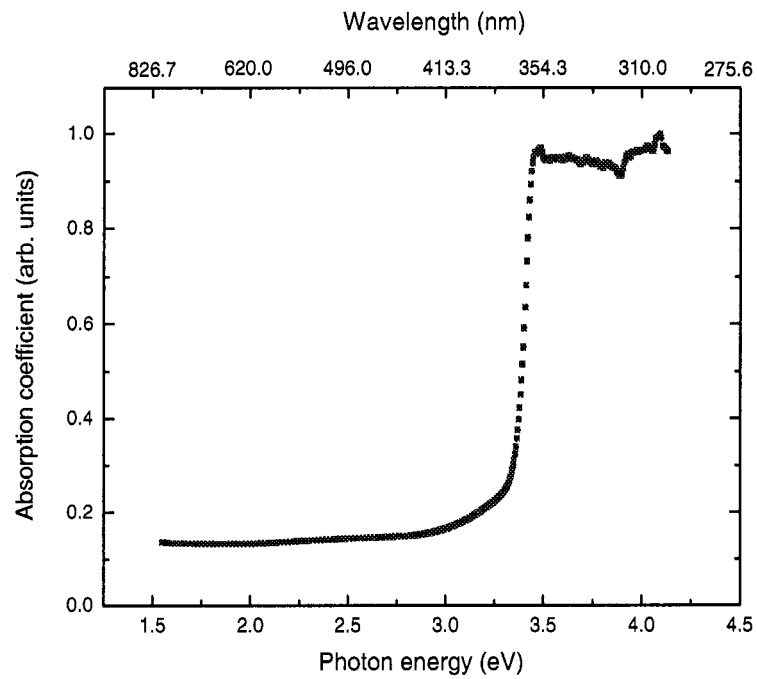
Fig. 2.4. Normalized absorption coefficient spectrum of our GaN single crystal.
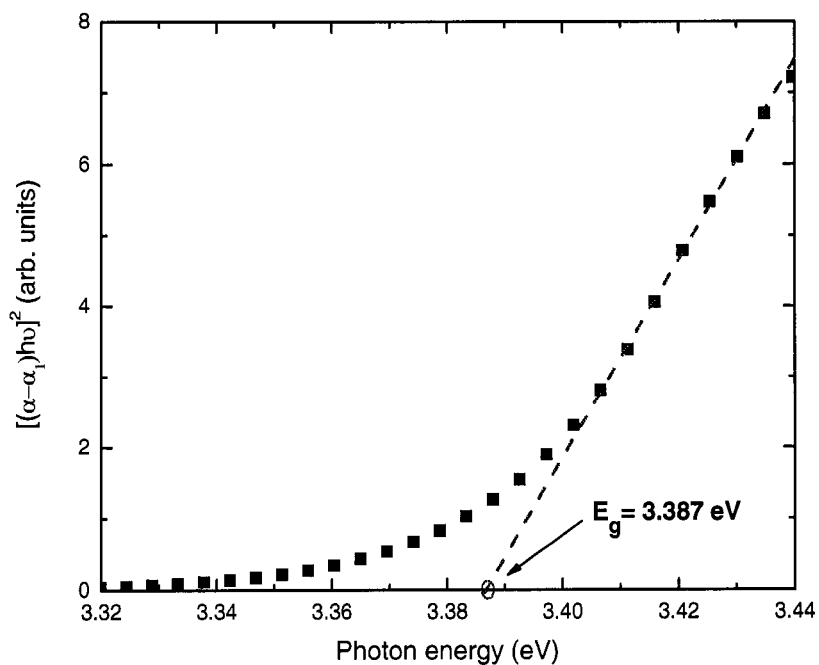
Fig. 2.5. Energy bandgap determination of GaN single crystal by absorption spectrum.

2.3 Pump-probe experiments

The two processes that we want to study: intervalley transitions and CAP dynamics, are both the ultrafast phenomena, taking place in a sub-picosecond or picosecond time range. Thus, we need an experimental tool, which possesses a sub-picosecond temporal resolution. The femtosecond pump-probe technique is an ideal candidate. This technique uses femtosecond laser pulses both for optical excitation and probing, simultaneously providing a timing gate for measurement events and acts

as a precise clock to control the generation and measurement of events. The pump-probe method has been the most frequent tool for investigating the ultrafast dynamics in semiconductors.

2.3.1 Principle of pump-probe experiment

The principle of pump-probe experiments is schematically shown in Fig. 2.6. A train of femtosecond optical pulses is split into two beams. One is the high-intensity pump beam, which is used to excite the sample under test and induce a transient change of the sample property (e.g., its reflectivity). The other is the low-intensity probe beam (a typical ratio of pump-to-probe powers is 10:1), which is used to monitor the pump-induced change. The probe beam is optically delayed with respect to the pump, which is realized through a computer-controlled delay line. When the delay line is at the position (1) in Fig. 2.6, the probe beam experiences a shorter optical path and arrives earlier than the pump beam on the sample. Since at this moment, the pump has not yet arrived, the probe does not see any change of the sample and its reflectivity or transmittance does not change too. When the delay line is moved from position (1) to (2), the probe and pump beams experience an equal-length optical path and arrive on the sample at the same time. The probe beam begins to experience the pump-induced change. This change is linearly related to the reflectivity or transmittance change of the probe beam. In the next cycle, the delay line is moved to position (3) and the probe beam has a longer optical path and arrives on the sample some time after the pump. Now the probe beam "sees" a given point of

the pump-induced transient. By repeating this process and plotting the reflectivity or transmittivity change of the probe beam as a function of the time delay between the two beams, one can map out the time-resolved pump-induced change of the sample. The pump-probe experiment is not a real-time measurement, so we need to assume that the transients induced by each pump pulse are identical.
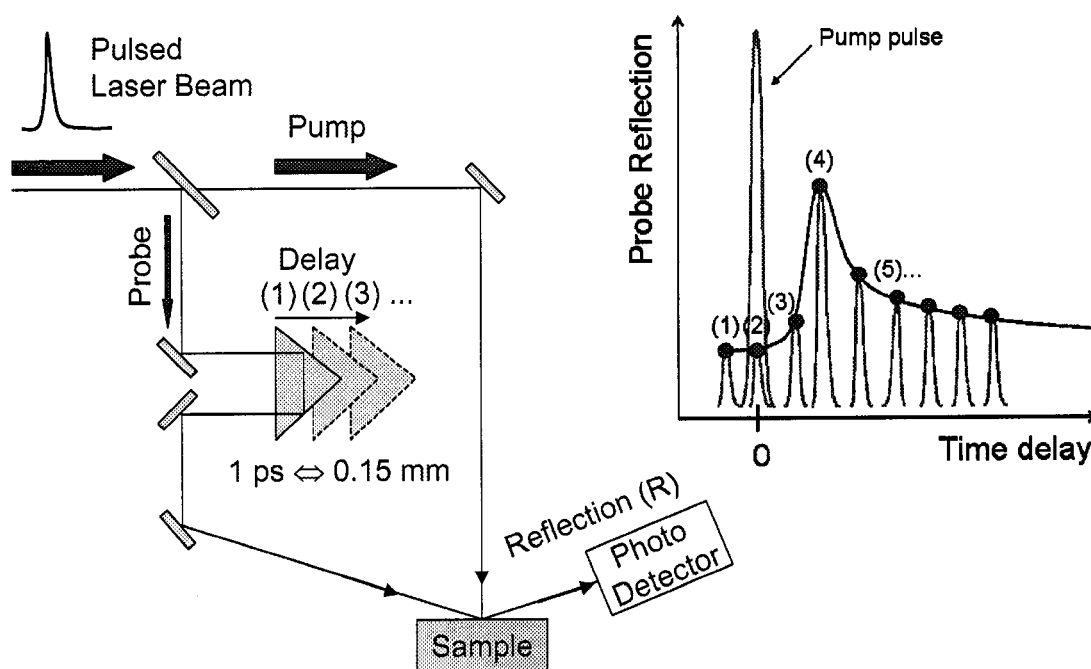
Fig. 2.6. Principle of the pump-probe experiments.

There are basically two types of pump-probe experiments, namely, degenerate and non-degenerate pump-probe. The degenerate pump-probe is also called one-color pump-probe and in this case the pump and probe beams have the same wavelength (color). In this configuration, the pump excites, e.g., free electrons from the valence band to a certain state of the conduction band and the probe monitors the electron density change of the same state, as shown in Fig. 2.7.
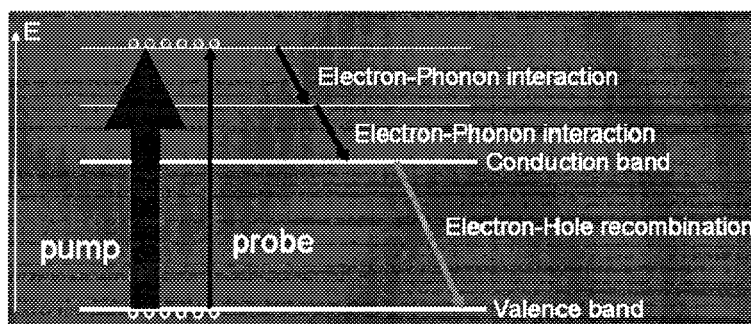
Fig. 2.7. Schematic diagram of a degenerate (one-color) pump-probe scheme.

In the non-degenerate pump-probe, or two-color pump-probe, one simultaneously uses two laser beams at different wavelengths (colors), which either come from two synchronized lasers, or one beam is generated by a nonlinear frequency conversion of the other one from the same laser source. The two-color configuration increases the versatility of the pump-probe technique tremendously, because now the probe can investigate energy states other than those optically-coupled by the pump.
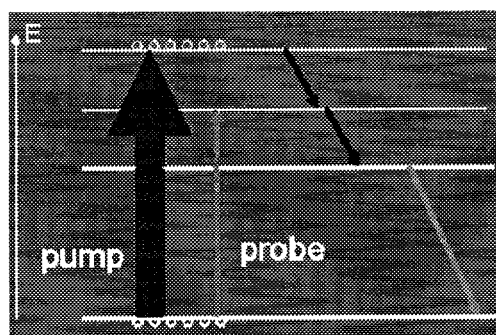
(a)
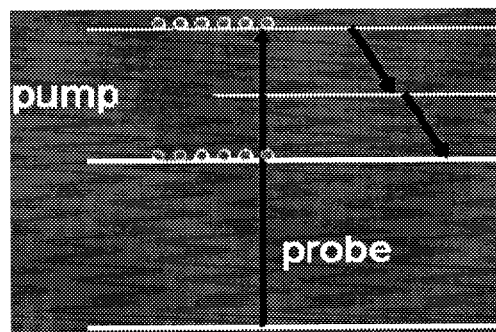
(b)
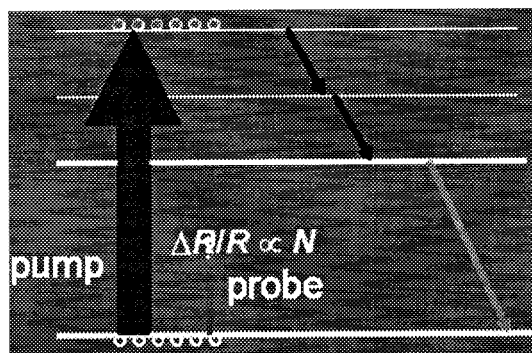
(c)

Fig. 2.8. Schematics of three non-degenerate (two-color) pump-probe techniques. (a): Both pump and probe are above-bandgap, but they have different wavelengths; (b): pump is below-bandgap and probe is above-bandgap; (c): pump is above-bandgap and probe is below-bandgap.

There are three different arrangements in non-degenerate pump-probe experiments, as shown in Fig. 2.8 (a), (b), and (c), respectively. In the first arrangement [Fig. 2.8(a)], both the pump and probe photons have the energy higher than the bandgap, but the state seen by the probe is different from the state populated by the pump excitation. Second arrangement [Fig. 2.8(b)] uses below-bandgap pump photons, while probes the states with above-bandgap photons. This arrangement is particularly useful for studies of n-type semiconductors. Since the pump photon energy is less than the bandgap, the pump cannot excite across the bandgap, however, for n-type samples, the below-bandgap pump efficiently heats the electrons already in the conduction band through the intraband excitation and induces a hot-electron distribution whose relaxation dynamics can then be monitored by the above-bandgap probe beam. The advantage of this arrangement against the one-color across-bandgap pump-probe configuration is that it allows for the direct measurement of the hot-electron relaxation dynamics without introducing any parasitic contribution of holes.

The third arrangement [Fig. 2.8(c)] is the above-bandgap pump and below-bandgap probe. In our work, this approach is utilized to study the intervalley scattering process, as well as for generation and detection of CAPs in GaN single crystals. Unlike the other pump–probe techniques mentioned above, where only the carrier population change occurring at a certain energy level can be monitored, the above-bandgap pump and below-gap probe experimental configuration monitors the total population change of electrons in the entire conduction band and does not depend on the details of the electronic states. As indicated in Refs. 6 and 7, for a

below-bandgap probe beam, the refractive index change Δn is purely induced by the photoexcited electron-hole plasma and can be described by the simple Drude model, which expresses Δn as

$$\Delta n / n = -\frac{2\pi e^2}{\varepsilon_0 \omega^2} \frac{N}{m^*},$$ (2.4)

where n is the refractive index of the sample at the probe wavelength, ε_0 is the background dielectric constant at low frequencies, e is the unit electronic charge, ω is the probe angular frequency, and N and m^* are the electron density and the effective mass in the conduction band, respectively. The contribution of holes to Δn is neglected, because holes typically have a much heavier effective mass than electrons. Equation (2.4) shows that Δn changes linearly with the density N of conduction-band electrons.

Since all our pump-probe experiments have been performed in the reflection mode, it is essential to show how the experimental probe-beam differential reflectivity $\Delta R/R$ is related to N. The definition of $\Delta R/R$ is

$$\Delta R / R = \frac{R'-R}{R},$$ (2.5)

where R' and R represent the probe beam reflectivity in the presence and absence of the pump beam, respectively. For thick samples, R at the normal incidence is defined as

$$R = \left[(n-1)/n+1 \right]^2 . \qquad (2.6)$$

Since R is only dependent on n, one can write $\Delta R/R$ as

$$\Delta R / R = d(\ln R)/dn \Delta n . \qquad (2.7)$$

By substituting Eq. (2.4) into the above equation, one can obtain the relationship between $\Delta R/R$ and N which is expressed as

$$\Delta R / R = -\frac{2\pi n e^2}{\varepsilon_0 \omega^2} \frac{d(\ln R)}{dn} \frac{N}{m^*} . \qquad (2.8)$$

Equation (2.8) shows that $\Delta R/R$ is linearly related to N. Therefore, the time-resolved $\Delta R/R$ signal directly gives the time evolution of N in the conduction band and does not depend on the details of the electronic states. This fact is essential to fully investigate the intervalley transitions of hot electrons, since the electrons transferred to the satellite valleys have a heavier effective mass and, as a result, reduced effective density.

Regarding the CAP dynamics studies, by using the probe beam with the photon energy far below the bandgap, we take advantage of a very small absorption coefficient (very weak attenuation) of the probe light in the sample and be able to demonstrate that CAP pulses propagate deeply into the material volume without any measurable loss of coherence. Another advantage of this configuration is that the below-bandgap probe is not sensitive to either the details of the band-gap structure or any interband absorption, which allows to avoid any undesired nonlinear effects and makes the studies of intervalley transitions and CAP dynamics very clear to interpret from the physics point of view. Finally, we also note that m^* enters into Eq. (2.8); thus, the above-bandgap pump and below-bandgap probe experiments can be also used to optically determine the carrier effective mass [8].

2.3.2 Femtosecond UV pump and NIR probe experimental setup

GaN is a direct-gap material, so UV laser pulses with photon energies above the GaN bandgap can directly excite electrons from the valence band to high-energy levels within the Γ-valley conduction band. Following the UV pump pulse, a time-delayed NIR probe pulse with the photon energy far below the bandgap, is guided to the same area on the sample surface and measures the relaxation dynamics of the excited hot electrons. As we have mentioned in Sec. 2.3.1, and will discuss in detail in Chaps. 3 and 4, our well-above-gap (UV) pump and far-below-gap (NIR) probe experimental configuration is very appropriate for the studies of intervalley scattering, as well as the behavior of CAPs in GaN.

Our experimental setup is schematically shown in Fig. 2.9. A passively mode-locked Ti:Sapphire pulsed laser is used to generate ~100 fs laser pulses at a repetition rate of 76 MHz. The pulse train from the laser is split by an 80/20 beam splitter into two beams. One is used to generate the UV pump pulses and the other is directly used as the probe beam. In our study, two arrangements are employed to generate the pump beam with the desired photon energy. One optical path (see Fig. 2.9) is designed to deliver photons with energies in the range of 3.10 to 3.54 eV (wavelength: 400 to 350 nm) in the vicinity of the GaN bandgap of 3.4 eV, and is based on frequency doubling of the fundamental Ti:sapphire pulse train using a β-BaB_2O_4 (BBO) crystal. The other includes our homemade third-harmonic generator [9] and enables us to generate pump photons with energies ranging from 4.38 eV to 4.71 eV (wavelength from 283 nm to 263 nm), far above the GaN bandgap. The pump beam, after passing through a UV-pass filter, is focused onto the surface of the GaN crystal with a spot diameter of ~20 μm at an incident angle of ~30°. The fluence incident on the sample surface is ~0.08 mJ/cm^2 per pulse and is kept constant while varying the pump photon energy. Probe pulses, directly generated by the Ti:sapphire laser, have photon energies varying from 1.46 eV to 1.77 eV (wavelengths from 850 nm to 700 nm), always far below the GaN gap and their fluence is always much lower (at least by a factor of 10) than that of the pump in order to ensure that the optical change in the material is induced by the pump photons only. The probe beam is delayed with respect to the pump by passing through a computer controlled delay line and near-normally incident on the same area on the sample surface with a spot

diameter of ~10 μm. The smaller spot size of the probe beam ensures that it probes a region with uniform photoexcitation and also relaxes the stringent requirement for the moving stage alignment. The probe reflection from the sample surface is filtered from any scattered pump photons by a NIR-pass filter and collected by a photodetector, which converts optical signals into electrical signals and then sends them to a lock-in amplifier. The lock-in amplifier is synchronized with a mechanical chopper that chops the pump beam at a frequency of ~2 KHz. The lock-in output is sent to a computer for data processing. The whole data acquisition system is controlled and synchronized by a LabView program running on the computer. The program controls the optical stage and when the stage reaches a stable speed, the data are taken from the lock-in amplifier. Meanwhile the computer calculates the corresponding stage position, the collected data are then automatically logged into a datafile and stored on a hard drive. Finally, a CCD camera is used to monitor beam focusing and overlapping on the sample. Our GaN single crystal can be placed in a cryostat, which allows us to perform both room-temperature and low-temperature measurements.
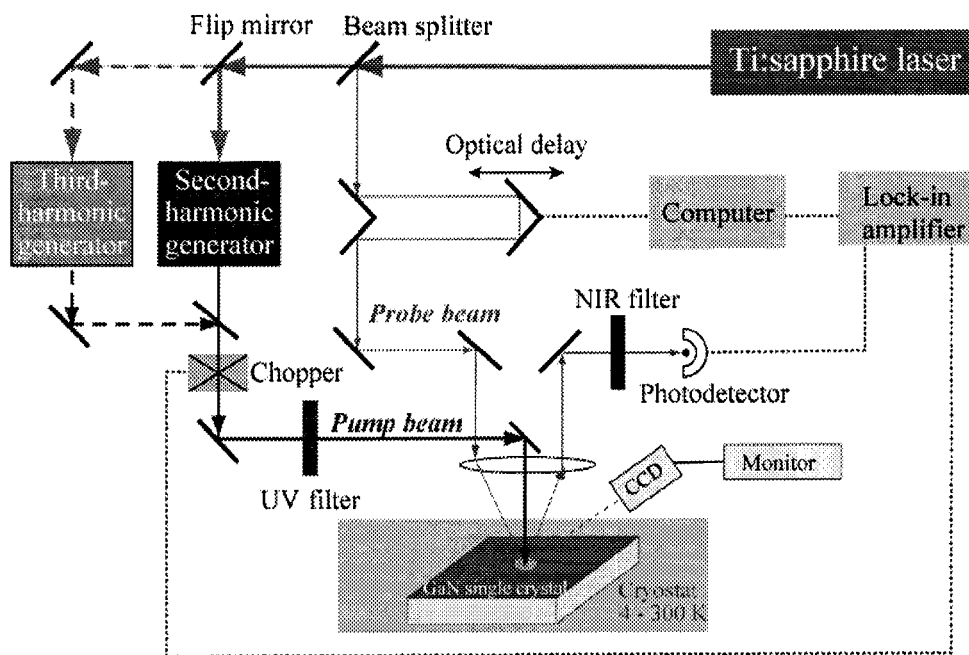
Fig. 2.9. Experimental setup for femtosecond UV pump-NIR probe spectroscopy.

References:

[1] J. Karpinski, J. Jun and S. Porowski, *J. Cryst. Growth* **66**, 1 (1984).

[2] J. Tauc, *Amorphous and Liquid Semiconductor*, **Chap.1**, Plenum Press, New York, 1981.

[3] S. Sirohi and T. P. Sharma, *Optical Materials* **13**, 267 (1999).

[4] V. Bougrov, M. E. Levinshtein, S. L. Rumyantsev and A. Zubrilov, in *Properties of Advanced SemiconductorMaterials GaN, AlN, InN, BN, SiC, SiGe* . **1-30**, Eds. M. E. Levinshtein, S. L. Rumyantsev and M. S. Shur, John Wiley & Sons, Inc., New York, 2001.

[5] M. Suzuki, T. Uenoyama and A. Yanase, *Phys. Rev. B* **52**, 8132 (1995).

[6] M. C. Downer and C. V. Shank, *Phys. Rev. Lett.* **56**, 761 (1986).

[7] F. E. Doany and D. Grischkowsky, *Appl. Phys. Lett.* **52**, 36 (1988).

[8] P. Perlin, E. Litwin-Staszewska, B. Suchanek, W. Knap, J. Camassel, T. Suski, R. Piotrzkowski, I. Grzegory, S. Porowski, E. Kaminska and J. C. Chervin, *Appl. Phys. Lett.* **68**, 1114 (1996).

[9] Doctoral thesis: *Ultrafast metal-semiconductor-metal UV photodetectors on gallium nitride*, by Jianliang Li, the University of Rochester (2004).

Chapter Three: Intervalley transition of hot electrons in GaN single crystals

Intervalley scattering, which is responsible for the transitions of electrons between the conduction band central valley and the satellite valleys, is not only an essential mechanism for excitation of free carriers in indirect-gap materials like Si or Ge, but also a very important scattering process of hot carriers in direct-bandgap semiconductors like GaAs or GaN. Once electrons are heated by an electric field or excited by an optical pulse, they reach energies in the central Γ valley equal to or greater than the Γ-L or Γ-A valley separations (L, A are the satellite valleys in the conduction band). Next, they can scatter by phonons and move from the Γ valley to the L or A valleys and vice versa. The phonons participating the intervalley scattering need to have a large wave number, which is close to the zone edge value to provide electrons enough momentum to transfer between Γ and L or A.

The Hamiltonian of the intervalley electron-phonon interaction is often expressed in terms of its matrix element between two electronic states:

$$\langle n_i, \vec{k}_i | H_{\text{intervalley}} | n_j, \vec{k}_j \rangle = D_{ij} u, \tag{3.1}$$

with D_{ij} known as the intervalley deformation potential. i and j denote the initial and final scattering valleys, respectively, n and $\bar{k}$ are the electron band index and wave vector, respectively, and u represents the phonon amplitude (the relative displacement of atoms). The electron wave vectors $\bar{k}_i$ and $\bar{k}_j$ are related to the phonon wave vector $\bar{q}$ by momentum conservation: $\bar{k}_j - \bar{k}_i = \bar{q}$. The intervalley scattering rate is determined by the Fermi golden rule and expressed as [1,2]:

$$\frac{1}{\tau_{ij}} = \frac{D_{ij}^2 Z_j m_j^{3/2}}{\sqrt{2}\pi\hbar^3\rho\omega_{ij}}[(N_{ij}+1)(\varepsilon - \hbar\omega_{ij} - \varepsilon_{0j})^{1/2} + N_{ij}(\varepsilon + \hbar\omega_{ij} - \varepsilon_{0j})^{1/2}], \quad (3.2)$$

where τ_{ij} is the phonon-assisted intervalley scattering time of electrons from the initial ith valley with the energy ε to the final jth valley, Z_j is the degeneracy of the jth valley, m_j is the effective mass of electrons in the jth valley, ρ is the density of the crystal, $\hbar\omega_{ij}$ is the phonon energy for the $i \rightarrow j$ intervalley scattering, N_{ij} is the number of intervalley scattering phonons, and, finally, ε_{0j} is the energy at the bottom of the jth valley. Equation (3.2) indicates that the scattering time from an initial state to a final state is related to the effective mass of the final state. The intervalley scattering is one of the ultrafast processes extensively studied in GaAs semiconductors [3-6] and typical time scales for GaAs are $\leq 200\,\mathrm{fs}$ for intervalley scattering from the central to the satellite valleys, and $\leq 2\,\mathrm{ps}$ for return to the central valley.

The direct temporal dynamics of the intervalley transitions in GaN has been poorly studied, because of the large energy separation between the central Γ valley and the satellite L and M valleys. Figure 3.1 schematically shows the band diagram of wurtzite GaN [7]. From the literature, we know that the second conduction-band minimum of the wurtzite GaN is located in the L valley [8-12]. According to the calculations of Rubio *et al.* [8], Suzuki *et al.* [9], and Palummo *et al.* [10], the energy separation between the L-valley point $L_{1,3}^c$ and the valence band point Γ_6^v is predicted to be 4.4 eV, 4.5 eV, or 4.54 eV, respectively.
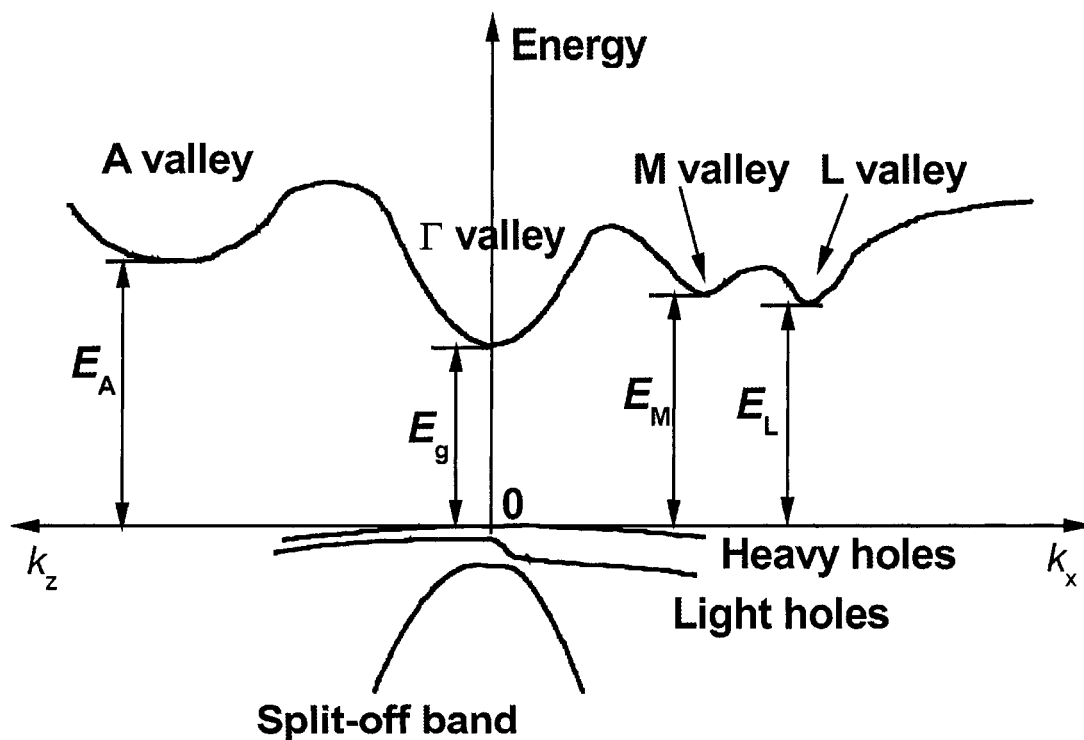
Fig. 3.1. Schematic band diagram of wurtzite GaN.

The reported intervalley scattering investigations performed in GaAs and other semiconductors presented in literature used either picosecond or femtosecond optical spectroscopy techniques [3-6, 13-17]. There are two main ways for initiating the intervalley transitions in time-resolved experiments. One method is to excite electrons from the bottom of the Γ band to upper energy states with below-bandgap infrared optical pulses via free carrier absorption and use the above-bandgap UV probe to monitor changes in the electron cooling behavior with and without the intervalley scattering [18]. This method was briefly discussed in Chap. 2 and schematically presented in Fig. 2.8(b), where we have stressed that it only works for n-doped samples and the observed transient signals are usually small because of a small free-carrier absorption cross section. The other method, discussed in Fig. 2.8(c), is a direct excitation of valence electrons to Γ valley high energy levels. When the excess energy of those highly excited electrons is greater than the energy separation between Γ and L, the intervalley scattering is enabled and electrons can transfer from Γ to L rapidly and then return within a longer time. As we demonstrated in Chap. 2, the latter method is a general approach, works not only for n-doped GaN, but also for undoped and p-doped crystals; the signals are large, as compared to the free-carrier-absorption mechanism, and physical interpretation of the results is quite straightforward.

In this chapter, I present our studies of intervalley transitions of hot electrons between the central Γ valley and the satellite L valley in bulk GaN single crystals using a femtosecond UV pump and NIR probe spectroscopy at both room and

cryogenic temperatures. The UV photons generated by our third-harmonic generator (THG) [see Fig. 2.9] produce very hot electrons with the energy in the vicinity of the threshold for the $\Gamma \leftrightarrow L$ scattering. The time evolution of the electron population in the Γ valley is monitored by measuring the $\Delta R/R$ signal of the NIR probe pulses. By tuning the pump wavelength across the intervalley scattering threshold, we observe a measurable change in the $\Delta R/R$ transient amplitude and rise time, due to the efficient transfer of electrons between the Γ and L valleys. Intrinsic time evolution of the L-valley electron population is obtained by subtracting the above-threshold pumping curve from the below-threshold pumping one. Our experimental results are interpreted using a solution of three-state rate equations, which yields the intervalley scattering times, optical phonon emission time, and deformation potential between Γ and L.

3.1 Experimental approach

GaN is a direct-gap material with bandgap energy of ~3.4 eV at room temperature, so UV laser pulses with photon energies above the gap can directly excite electrons from the valence band to high-energy levels within the Γ-valley conduction band. Following the UV pump pulse, a time-delayed NIR probe pulse with photon energy far-below the bandgap, is guided to the same area on the sample surface and monitors the relaxation dynamics of the excited hot electrons. Our well-above-gap (UV) pump and far-below-gap (NIR) probe experimental configuration is

particularly suitable for studies of time-resolved intervalley transition processes for the following reasons:

1. The NIR probe is not sensitive to either the details of the band-gap structure or any interband absorption.

2. Free-carrier absorption, which is the main intraband absorption mechanism in GaN for the below-gap wavelength range, can be neglected because of a very small, ~50 cm^{-1}, absorption coefficient of ~800-nm light in GaN crystals [19].

3. The possibility of the two-photon-absorption process is also negligible, because the total energy of two ~800-nm probe photons is still considerably lower than the GaN bandgap energy.

4. The NIR probe beam can monitor the total population change of electrons in the entire conduction band, as was earlier indicated in Eq. (2.8), and this last property is essential to obtain the full picture of the time-resolved intervalley transition process in GaN.

Equation (2.8) shows a general relationship between the $\Delta R/R$ signal of the probe beam and the conduction band total electron density N. Without the intervalley transition, N simply represents the electron density in the central Γ valley. However, once we include the intervalley transition process, we need to modify (2.8) by substituting $N_\Gamma/m_\Gamma^* + N_L/m_L^*$ for N/m^*, where N_Γ, N_L, m_Γ^*, and m_L^* denote N and m^* in the Γ and L valleys, respectively, since in GaN the electrons transferred to

the L valley have a heavier effective mass and, as a result, reduced effective density.

It is convenient to introduce an effective electron density N_{eff}, defined as

$$N_{eff} = N_{\Gamma} + \left(m_{\Gamma}^* / m_{L}^* \right) N_{L} \tag{3.3}$$

to transform Eq. (2.8) into the final, "experimentalist friendly" form:

$$\Delta R / R = -\frac{2\pi n_0 e^2}{\varepsilon_0 \omega^2} \frac{d\left(\ln R\right)}{dn} \frac{N_{eff}}{m^*}. \tag{3.4}$$

We stress that based on (3.4) the $\Delta R/R$ time evolution that we measure in our experiments gives us the time evolution of N_{eff} directly, as within our experimental tuning range, changes in n_0, corresponding to the different probe frequencies, are small and their impact on $\Delta R/R$ is negligible. From the definition of N_{eff} [Eq. (3.3)], its time evolution actually reflects the transfer of electrons between the Γ and L valleys.

The above discussion shows that our UV–NIR, two-color femtosecond pump-probe spectroscopy allows us to avoid any undesired effects and makes our intervalley transition studies in GaN very straightforward to interpret.

3.2 Experimental results

Our experimental setup for the two-color (UV–NIR) femtosecond spectroscopy has been described in Chap. 2. A GaN single crystal was placed in a cryostat for both room-temperature and low-temperature measurements. For the intervalley transition studies, the UV pulses from our THG system were used as the pump to excite our GaN sample and the probe beam $\Delta R/R$ transients at different pump photon energies were collected. We note that within the energy tuning range of our THG system (4.38–4.71 eV, corresponding wavelength range: 263–283 nm), the only possible intervalley transition process was the $\Gamma \leftrightarrow L$ transition. Scattering of electrons from the Γ valley to the bottom of the M valley could not be initiated, since the separation energy between the M-valley bottom and the valence band point Γ_6^v is ≥ 5.02 eV at room temperature [8, 9] and even larger at low temperatures.

3.2.1 Experimental results for room-temperature measurements

At room temperature, we have collected the probe-beam, time-resolved $\Delta R/R$ transients in the tuning range of the pump beam, where we expected that the $\Gamma \leftrightarrow L$ transition threshold should lie. Figure 3.2(a) presents four representative $\Delta R/R$ waveforms measured at pump-photon energies of 4.64 eV (solid line), 4.59 eV (dash-dotted line), 4.48 eV (dashed line), and 4.38 eV (dotted line) (wavelengths of 267 nm, 270 nm, 277 nm, and 283 nm, respectively), while Fig. 3.2(b) shows the same curves, but normalized to their peak values to compare the transients' rise times. It can be

seen from both figures that our four waveforms can be grouped into two distinct groups. The curves for the 4.48-eV and 4.38-eV excitations (Group I) have larger amplitudes [Fig. 3.2(a)] and, correspondingly, longer rise times [Fig. 3.2(b)]. At the same time, the amplitudes of the curves for the 4.64-eV and 4.59-eV excitations (Group II) are smaller and their rise times are shorter. These differences in the peak values and the rise times between the curves in the Group I and II indicate that the intervalley-scattering threshold in the GaN material should lie somewhere between 4.48 eV and 4.59 eV. The inset in Fig. 3.2(a) shows the $\Delta R/R$ time evolution on a longer, 20-ps time-scale, demonstrating that after the initial split, the curves belonging to both groups merge.

Fig. 3.2. Time-resolved ΔR/R waveforms measured in GaN single crystals at room temperature for pump-photon energies of 4.64 eV (solid line), 4.59 eV (dash-dot line), 4.48 eV (dashed line), and 4.38 eV (dotted line) (corresponding wavelengths are 267 nm, 270 nm, 277 nm, and 283 nm, respectively). The NIR probe wavelengths were, correspondingly, 801 nm, 810 nm, 831 nm, and 849 nm. (a) Actually collected ΔR/R transients, normalized to the trace obtained for the 4.38-eV pump photons. (b) The ΔR/R transients from (a) independently normalized to their peak values. The inset in (a) shows the same transients, but presented in the long, 20-ps-wide time window.

To exactly determine the position of the $\Gamma \leftrightarrow L$ transition threshold, we plotted the $\Delta R/R$ amplitude [Fig. 3.3(a)] and the rise time [Fig. 3.3(b)] dependences on the pump-photon energy for all transients we measured. Both data sets are shown in Fig. 3.3 and clearly demonstrate a threshold-like behavior, indicated by the solid lines, which are the best step-function–type numerical fits to our data. The inflection point has the energy value of 4.51±0.01 eV, as marked in Fig. 3.3 by thin dashed lines. The amplitude and rise time differences above and below the 4.51-eV threshold are well above our experimental error and show the $\Gamma \leftrightarrow L$ intervalley transition structure.

With the below-threshold excitation, electrons cannot transfer from Γ to L, thus, $N_L = 0$ and $N_{\text{eff}} = N_\Gamma$. When the pump-photon energy is tuned above the threshold, the $\Gamma \leftrightarrow L$ transition is enabled and a large fraction of electrons originally excited into the Γ valley transfer to the L valley. Since $m_L^* > m_\Gamma^*$ ($m_L^* \approx 0.4\,m_e$ and $m_\Gamma^* \approx 0.2\,m_e$ in wurtzite GaN [20, 21], where m_e is the free-electron mass), for the same pump fluence, N_{eff} is initially measurably reduced for the above-threshold excitation in comparison with the below-threshold excitation. On the other hand, at longer delay times [see inset in Fig. 3.2(a)], the backscattering of electrons from L to Γ repopulates the Γ valley and the $\Delta R/R$ traces belonging to Groups I and II merge. From (3.4) we can calculate that for a 1-ps delay time, $N_\Gamma : N_L \approx 1:1$, which means that within the first picosecond about 50% of photoexcited electrons have transferred from Γ to L.
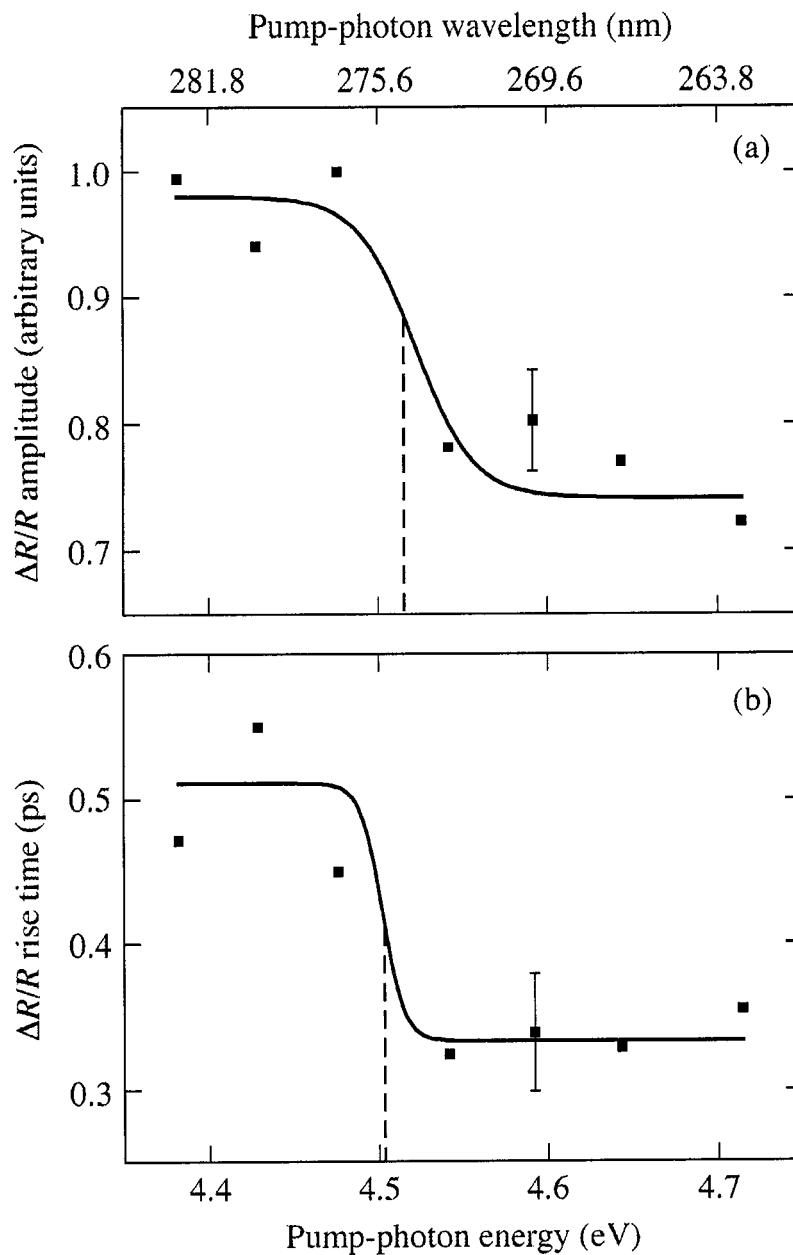
Fig. 3.3. The amplitudes (a) of the $\Delta R/R$ waveforms shown in Fig. 3.2(a) and the rise times (b) of the $\Delta R/R$ waveforms shown in Fig. 3.2(b) versus the pump-photon energy. The representative error bar is shown for the 4.59-eV data. The solid lines were obtained as the best step-like function fits, but should be regarded mainly as guides to the eye. The thin dashed lines indicate the value of the intervalley energy threshold at room temperature.

We note in Figs. 3.2(b) and 3.3(b) that the Group II curves, which include the intervalley scattering, exhibit measurably shorter rise times than those without the intervalley scattering (Group I). If we assume the rising edge of the $\Delta R/R$ waveforms belonging to Group I simply reflects the pump-beam energy delivery rate to our system, the intervalley scattering notably speeds up the pumping process, and the $\Gamma \rightarrow L$ scattering time can be estimated as ~180 fs, the difference in the rise times of the $\Delta R/R$ transients belonging to the Groups I and II [Fig. 3.3(b)]. We note that this latter value is just the upper limit, as it is limited by the width of our pump pulse.

The return time of electrons from L to Γ is much longer than the $\Gamma \leftrightarrow L$ scattering time, and corresponds to the $\Delta R/R$ transient decay, shown in the inset in Fig. 3.2(a). The inset shows that all four $\Delta R/R$ curves merge at the delay time of ~20 ps, which is the time when all L-valley electrons return the Γ valley. This experimental L-valley depopulation time should not be, however, confused with the much shorter $L \rightarrow \Gamma$ scattering time, which is actually associated with the optical phonon emission process, as we demonstrate later using the rate-equation analysis.

3.2.2 Experimental results for measurements at 100 K

It is well known that the value of the energy bandgap of semiconductors typically increases as the temperature is decreased. For example, the energy bandgap of GaN is ~3.39 eV at 300 K, ~3.46 at 100 K and ~3.47 eV at ~0 K [22]. Although the temperature dependence of the separation energy between the L valley and the

valence band is unknown for GaN, we expect it to follow the same trend. This implies that the energy threshold for the $\Gamma \leftrightarrow L$ transition should be greater at low temperatures than that at room temperature. By repeating our experiments at low temperature, we could not only confirm the dynamics of the intervalley transition process in GaN, but also reveal how the energy threshold shifts and how the relevant scattering times change.

Our low temperature experiments were performed at 100 K by keeping other experimental conditions unchanged with respect to the room temperature experiments. Figure 3.4 shows the low-temperature versions of the four $\Delta R/R$ waveforms presented in Fig. 3.2. Essentially identical features are found by comparing Fig. 3.4 with Fig. 3.2:

(1)   the waveforms can be grouped into two distinct groups in terms of their peak values and rise times and Group I (curves for the 4.48-eV and 4.38-eV excitations) have larger amplitudes [Fig. 3.4(a)] and, correspondingly, longer rise times [Fig. 3.4(b)], as compared to Group II (curves for the 4.64-eV and 4.59-eV excitations);

(2)   all curves belonging to both groups merge on a longer ~20-ps time-scale, as shown in the inset in Fig. 3.4(a). These features clearly demonstrate the efficient intervalley transition also occurs at the temperature of 100 K.

In analogy to Fig. 3.3, we also plotted the $\Delta R/R$ amplitude and rise time dependences on the pump-photon energy for all transients we measured at 100 K, as shown in Fig. 3.5 (a) and 3.5 (b), respectively. Again, both data sets clearly

demonstrate a threshold-like behavior. The threshold energy, as indicated by the inflection point, is 4.57±0.01 eV. It means the pump-photon energy must be higher than 4.57 eV in order to initiate the $\Gamma \leftrightarrow L$ intervalley transition at 100 K. The shift of the energy threshold from 4.51 eV to 4.57 eV also indicates that the energy separation between the valence band and the conduction band L valley increases by 0.06 eV, when the temperature changes from room temperature to 100 K. As we know, the $E_g(T)$ dependence in direct bandgap semiconductors is well described by the Varshni relation [23]:

$$E_g(T) = E_g(0) - \frac{\gamma T^2}{T + \beta}, \qquad (3.5)$$

where $E_g(0)$ is E_g at 0 K; β is a constant associated with the Debye temperature; and γ is an empirical constant. For GaN, $E_g(0) = 3.47\,\text{eV}$, $\beta = 600\,\text{K}$ and $\gamma = 7.7 \times 10^{-4}$ eV/K [22]. If we assume the energy separation between the valence band and the L valley also follows the Varshni law, we can predict that the band separation should increase by 0.066 eV, when the temperature decreases from 300 K to 100 K. Thus, our experimentally obtained 0.06-eV shift is in a very good agreement with the Varshni formula.
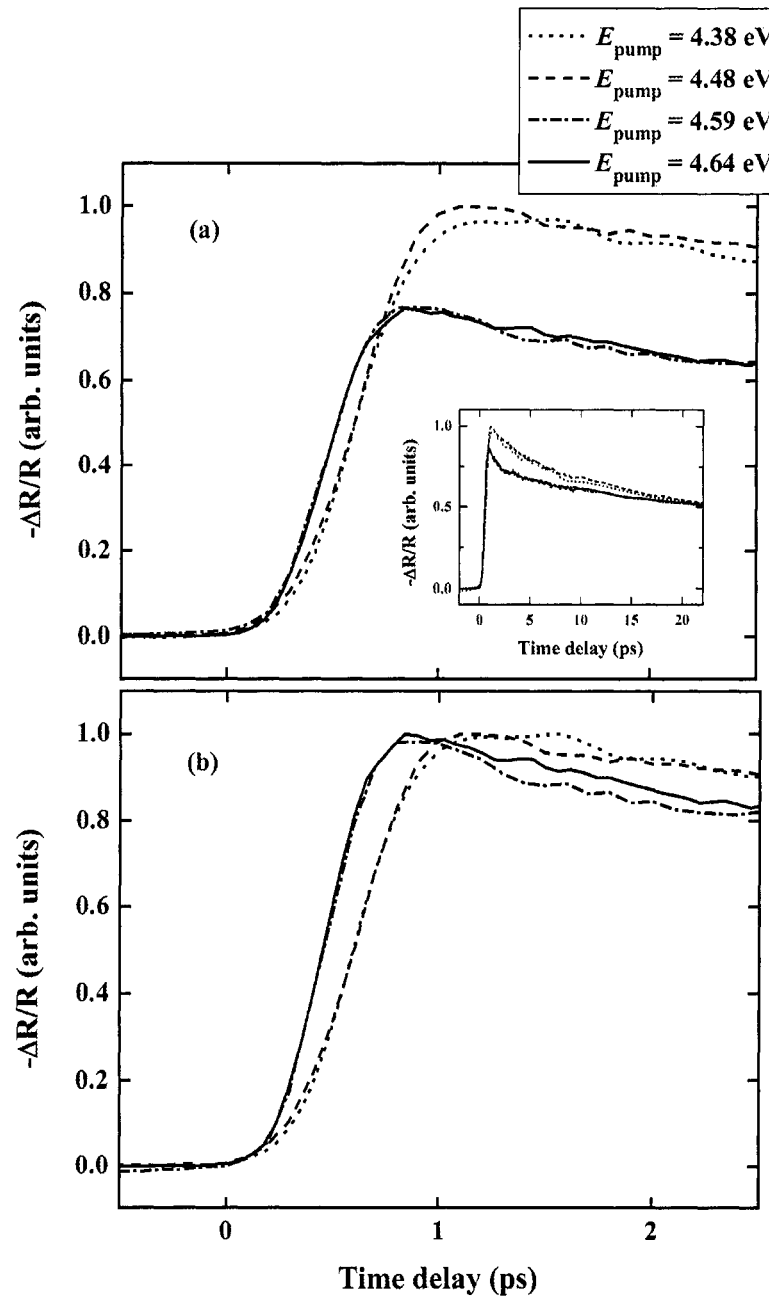
Fig. 3.4. Time-resolved $\Delta R/R$ waveforms measured in GaN single crystals at the temperature of 100 K for pump-photon energies of 4.64 eV (solid line), 4.59 eV (dash-dot line), 4.48 eV (dashed line), and 4.38 eV (dotted line) (corresponding wavelengths are 267 nm, 270 nm, 277 nm, and 283 nm, respectively). The NIR probe wavelengths were, correspondingly, 801 nm, 810 nm, 831 nm, and 849 nm. (a) Actually collected $\Delta R/R$ transients, normalized to the trace obtained for the 4.38-eV pump photons. (b) The $\Delta R/R$ transients from (a) independently normalized to their peak values. The inset in (a) shows the same transients, but presented in the long, 20-ps-wide time window.
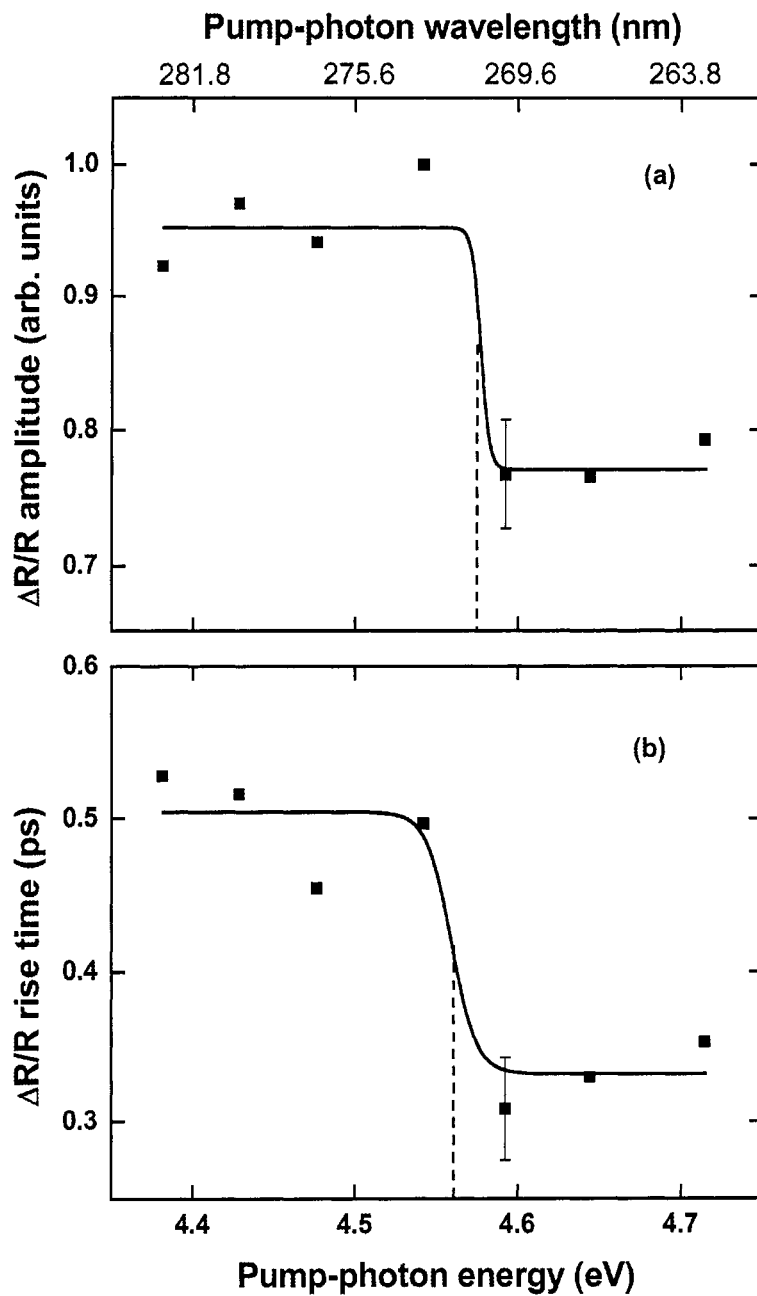
Fig. 3.5. The amplitudes (a) of the $\Delta R/R$ waveforms shown in Fig. 3.4 (a) and the rise times (b) of the $\Delta R/R$ waveforms shown in Fig. 3.4(b) versus the pump-photon energy. The representative error bar is shown for the 4.59-eV data. The solid lines were obtained as the best step-like function fits, but should be regarded mainly as guides to the eye. The thin dashed lines indicate the value of the intervalley energy threshold at 100 K.

3.3. Theoretical modeling and experimental fitting

The $\Gamma \to L$ and $L \to \Gamma$ scattering times, as well as the optical phonon emission time, can be extracted from our experimental data by solving the intervalley transition rate equations and then fitting the solution to the time-resolved $N_L(t)$ derived from the $\Delta R/R$ transients [see Eq. (3.4)]. As we have demonstrated, there exists an energy threshold within the Γ valley, below which the electrons can no longer scatter into the L valley. Thus, we can separate the states within the Γ valley into Γ^+ and Γ^- states, where Γ^+/Γ^- denote the electron states with energies above/below the threshold, respectively. The electrons in the L valley are in the third separate state that is labeled by L.

The three-state rate equations governing the dynamics of the hot-electron N_{Γ^+}, N_{Γ^-}, and N_L populations (densities) in the Γ^+, Γ^-, and L electronic states, and coupled through both the $\Gamma \leftrightarrow L$ intervalley and $\Gamma^+ \leftrightarrow \Gamma^-$ intravalley scatterings, can be written as

$$\frac{d}{dt}\begin{bmatrix} N_{\Gamma^+}(t) \\ N_L(t) \\ N_{\Gamma^-}(t) \end{bmatrix} = \begin{bmatrix} \dfrac{I(t)\alpha}{h\nu} & -\left(\dfrac{1}{\tau_{\Gamma L}} + \dfrac{1}{\tau_{op}}\right) & \dfrac{1}{\tau_{L\Gamma}} & 0 \\ 0 & \dfrac{1}{\tau_{\Gamma L}} & -\dfrac{1}{\tau_{L\Gamma}} & 0 \\ 0 & \dfrac{1}{\tau_{op}} & 0 & 0 \end{bmatrix} \begin{bmatrix} 1 \\ N_{\Gamma^+}(t) \\ N_L(t) \\ N_{\Gamma^-}(t) \end{bmatrix}, \qquad (3.6)$$

where α is the band-to-band absorption coefficient, $I(t)$ is the incident intensity of the pump-pulse light with the photon energy $h\nu$, $\tau_{\Gamma L}$ is the $\Gamma \rightarrow L$ scattering time, $\tau_{L\Gamma}$ is the $L \rightarrow \Gamma$ scattering time, and τ_{op} is the time of $\Gamma^+ \leftrightarrow \Gamma^-$ scattering, which is limited by the optical phonon emission in the Γ valley. We also note that $N_{\Gamma^+} + N_{\Gamma^-} = N_\Gamma$, as electrons in the L valley can only scatter into the Γ^+ states. Finally, for simplicity, we ignore the electron-hole recombination process, because it is of the order of several hundred picoseconds [24] in GaN and is much slower than any scattering transitions times discussed here.

The three-state rate-equation model presented in Eq. (3.6) was introduced earlier in Ref. 25 for GaAs and InP compound semiconductors. Here, we added the excitation term $I\alpha/h\nu$, as we observed experimentally that $\tau_{\Gamma L}$ was comparable to the pump-pulse width in our case. We solved Eq. (3.6) numerically for N_{Γ^+}, N_{Γ^-} and $N_L(t)$, taking into account that $\tau_{\Gamma L}$ and $\tau_{L\Gamma}$ are not independent, but related through Eq. (3.2) which indicates that the scattering time from an initial state to a final state is related to the effective mass of the final state. For wurtzite GaN, the energy of intervalley phonons $\hbar\omega_{\Gamma L} \approx 92$ meV (see Ref. 21) and $\varepsilon_{0\Gamma^+}$ is the 4.51-eV intervalley threshold at 300 K; thus, $\varepsilon_{0L} = \varepsilon_{0\Gamma^+} + \hbar\omega_{\Gamma L} \approx 4.6$ eV. Accounting for the nonparabolicity of the Γ valley and the sixfold degeneracy of the L valley [20,21], we get $\tau_{\Gamma L}/\tau_{L\Gamma} \approx 1/10$ for 4.64-eV (267-nm) photoexcitation.

The solutions for $N_L(t)$ (solid lines), along with the room-temperature experimental data (dots) are shown in Fig. 3.6. The experimental points in Fig. 3.6 were obtained by numerical subtractions of the traces which include the intervalley scattering from the traces measured below the transition threshold [Figure 3.6 (a) corresponds to the 4.48-eV trace minus the 4.64-eV trace, (b) 4.48-eV – 4.59-eV, and (c) 4.38-eV – 4.59-eV, respectively]. Performing the subtractions we assumed that the hypothetical 4.64-eV and 4.59-eV curves without the intervalley scattering must be very similar (small energy difference of the pump) to the actual experimentally measured 4.48-eV and 4.38-eV $\Delta R/R$ waveforms. The subtraction eliminated any undesired hot electron relaxation processes and gave us directly the time evolution of the L-valley electron population, as indicated in Eq. (3.4). We note an excellent agreement between our experimental results and the rate-equation fits. We also stress that a similarly good agreement was obtained by subtracting any two $\Delta R/R$ traces between the Group I and II and no pump-photon energy dependence was observed.

Within our experimental error, the fitted values of $\tau_{L\Gamma}$ and τ_{op} were the same in all cases. The latter can be explained by looking at Eq. (3.2). Since both $\Gamma \rightarrow L$ and optical-phonon scattering times are shorter than the $L \rightarrow \Gamma$ time, the electrons transferred to the L valley would first relax down to the bottom of the L valley through optical phonon scattering and then return to the Γ^+ state via $L \rightarrow \Gamma$ transfer. Thus, the electron energy that determines the $\tau_{L\Gamma}$ value in Eq. (3.2) is the energy of the bottom of the L valley, which is fixed. Therefore, $\tau_{L\Gamma}$ cannot change with the

pump-photon energy, as was, in fact, confirmed earlier in Ref. 26. Similarly, τ_{op} can

have only a very weak dependence on the excess energy.

Using the least squares fits for all traces shown in Fig. 3.6, we obtained an

average $\tau_{L\Gamma}$ equal to 1.02±0.25 ps and an average $\tau_{op} = 0.29 \pm 0.06\,\mathrm{ps}$, and, then,

determined $\tau_{\Gamma L}$ to be ~100 fs, in good agreement with our experimental, ~180 fs

estimate based on Fig. 3.3(b). Our value for $\tau_{L\Gamma}$ is also in good agreement with Sun's

report [18], while τ_{op} is close to the 200-fs value reported in Ref. 27. As we

mentioned earlier, the ~1 ps $L \rightarrow \Gamma$ scattering time is much faster than the total

depopulation time of the L valley, which was measured to be ~20 ps [see inset in Fig.

3.2(a)].

Finally, we obtained the deformation potential between the Γ and L valleys

from Eq. (3.2) for the fixed $\tau_{L\Gamma} = 1.02$ ps and other parameters listed in Refs. 20 and

21. Our $D_{\Gamma L} \approx 0.92 \times 10^9$ eV/cm value agrees very well with the one $(1.0 \times 10^9$

eV/cm) reported by Bhapkar and Shur [20].
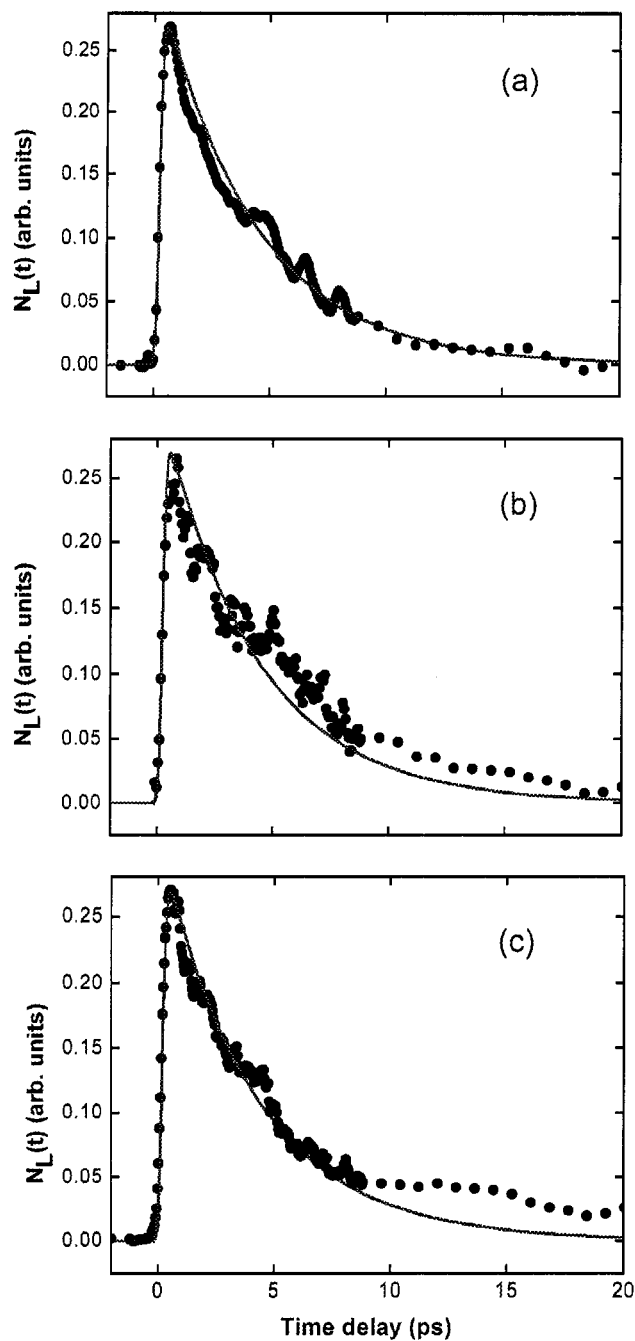
Fig. 3.6. Time evolution of the $N_L(t)$ population at room temperature. The dots in (a), (b) and (c) are experimental data obtained by subtracting the 4.64-eV $\Delta R/R$ trace from the 4.48-eV trace, the 4.59-eV $\Delta R/R$ trace from the 4.48-eV trace, and the 4.59-eV $\Delta R/R$ trace from the 4.38-eV trace, respectively. The solid lines in (a), (b) and (c) are the numerical solutions of our three-state rate equations [Eq. (3.6)].

We have also applied the same fitting procedure to our 100-K experimental

data, and have found a good agreement between our experimental results and the rate-

equation fits. Figure 3.7 shows the representative fitting result. The experimental

points were obtained by subtracting the 4.64-eV $\Delta R/R$ trace from the 4.48-eV trace.

The solid line is the rate-equation fit. The values of $\tau_{L\Gamma} = 1.06 \pm 0.18$ ps and

$\tau_{op} = 0.35 \pm 0.09$ ps obtained from the least squares fits here were, within the

experimental error, actually the same as the room-temperature values.
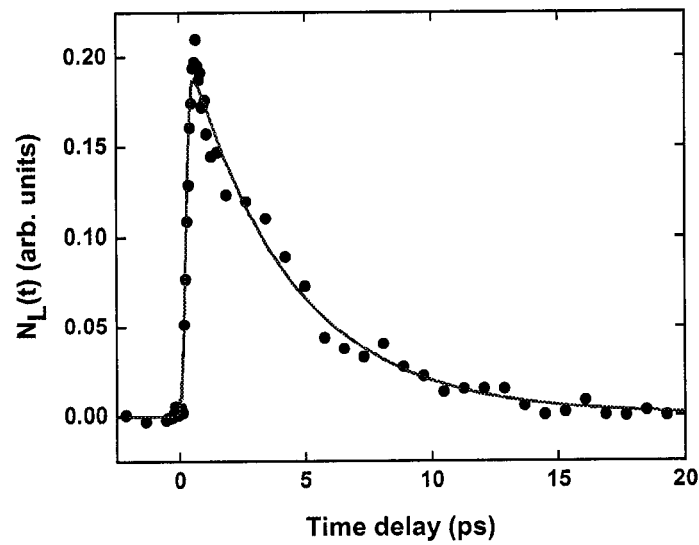
Fig. 3.7 Time evolution of the $N_L(t)$ population at 100 K. The dots are experimental data obtained by subtracting the 4.64-eV $\Delta R/R$ trace from the 4.48-eV trace. The solid line is the numerical solution of our three-state rate equations [Eq. (3.6)].

3.4. Conclusions

In Chap. 3, we have presented our detailed studies of the intervalley scattering of hot electrons in high-quality bulk GaN crystals using UV-pump and NIR-probe $\Delta R/R$ femtosecond spectroscopy technique at both room temperature and 100 K. The two-color, pump–probe configuration allowed us to directly observe the time-resolved electron population change in the Γ and L valleys. The pump-photon energy-dependent measurements demonstrated that the energy threshold for the $\Gamma \leftrightarrow L$ transition was 4.51 eV at room temperature and 4.57 eV at 100 K. The three-state rate equations, modified to include the finite width of our pump pulses, were solved numerically and their solution fitted extremely well our experimental data. From the fit, we determined that the characteristic time constants, defining the dynamics of both the $\Gamma \leftrightarrow L$ intervalley and $\Gamma^+ \leftrightarrow \Gamma^-$ intravalley transitions, were, within our tested range, independent of the pump-photon energy and temperature, and their values were $\tau_{L\Gamma} \approx 1$ ps, $\tau_{\Gamma L} \approx 100$ fs, and $\tau_{op} \approx 300$ fs. The deformation potential between the two valleys was 0.92×10^9 eV/cm. As compared to the $\Gamma \leftrightarrow L$ intervalley scattering in GaAs, where $\tau_{\Gamma L} \sim 50$ fs and $\tau_{L\Gamma} \sim 500$ fs (Ref. 25), the carrier dynamics in GaN is approximately two times slower.

References:

[1]   E. M. Conwell and M. O. Vassell, *IEEE Trans. Electron Devices* **ED-13**, 22 (1966).

[2]   S. Zollner, S. Gopalan, and M. Cardona, *Appl. Phys. Lett.* **54**, 614 (1989).

[3]   P. C. Becker, H. L. Fragnito, C. H. Brito Cruz, J. Shah, R. L. Fork, J. E. Cunningham, J. E. Henry and C. V. Shank, *Appl. Phys. Lett.* **53**, 2089 (1988).

[4]   J.-Y. Bigot, M. T. Portella, R. W. Schoenlein, J. E. Cunningham and C. V. Shank, *Phys. Rev. Lett.* **65**, 3429 (1990).

[5]   J. Shah, B. Deveaud, T. C. Damen, W. T. Tsang, A. C. Gossard and P. Lugli, *Phys. Rev. Lett.* **59**, 2222 (1987).

[6]   P. N. Saeta, J. F. Federici, B. I. Greene and D. R. Dykaar, *Appl. Phys. Lett.* **60**, 1477 (1992).

[7]   M. Suzuki, T. Uenoyama and A. Yanase, *Phys. Rev. B* **52**, 8132 (1995).

[8]   A. Rubio, J. L. Corkill, M. L. Cohen, E. L. Shirley and S. G. Louie, *Phys. Rev. B* **48**, 11,810 (1993).

[9]   M. Suzuki and T. Uenoyama, *Jpn. J. Appl. Phys.* **34**, 3442 (1995).

[10] M. Palummo, C. M. Bertoni, and F. Finocchi, *Physica B* **185**, 404 (1993).

[11] Y. C. Yeo, T. C. Chong and M. F. Li, *J. Appl. Phys.* **83**, 1429 (1998).

[12] G. L. Zhao, D. Bagayoko and T. D. Williams, *Phys. Rev. B* **60**, 1563 (1999).

[13] D. J. Dougherty, S. B. Fleischer, E. L. Warlick, J. L. House, G. S. Petrich, L. A. Kolodziejski and E. P. Ippen, *Appl. Phys. Lett.* **71**, 3144 (1997).

[14] S. K. O'Leary, B. E. Foutz, M. S. Shur and L. F. Eastman, *Solid State Commun.* **118**, 79 (2001).

[15] L. H. F. Andrade, R. E. Marotti, A. A. Quivy and C. H. de Brito Cruz, *Solid State Commun.* **121**, 181 (2002).

[16] M. C. Nuss, D. H. Auston, and F. Capasso, *Phys. Rev. Lett.* **58**, 2355 (1987).

[17] W. B. Wang, K. Shum, R. R. Alfano, D. Szmyd and A. J. Nozik, *Phys. Rev. Lett.* **68**, 662 (1992).

[18] C.-K. Sun, Y.-L. Huang, S. Keller, U. K. Mishra and S. P. DenBaars, *Phys. Rev. B* **59**, 13,535 (1999).

[19] G. Yu, G. Wang, H. Ishikawa, M. Umeno, T. Soga, T. Egawa, J. Watanabe and T. Jimbo, *Appl. Phys. Lett.* **70**, 3209 (1997).

[20] U. V. Bhapkar and M. S. Shur, *J. Appl. Phys.* **82**, 1649 (1997).

[21] J. C. Cao and X. L. Lei, *Eur. Phys. J. B* **7**, 79 (1999).

[22] V. Bougrov, M. E. Levinshtein, S. L. Rumyantsev and A. Zubrilov, in *Properties of Advanced SemiconductorMaterials GaN, AlN, InN, BN, SiC, SiGe* . **1-30**, Eds. M. E. Levinshtein, S. L. Rumyantsev and M. S. Shur, John Wiley & Sons, Inc., New York, 2001.

[23] Y. P. Vashni, *Physica* **34**, 149 (1967).

[24] M. Wraback, H. Shen, C. J. Eiting, J. C. Carrano and R. D. Dupuis, *MRS Internet J. Nitride Semicond. Res.* **5S1**, W11.55 (2000).

[25] C. J. Stanton and D. W. Bailey, *Phys. Rev. B* **45**, 8369 (1992).

[26]   J. Y. Duboz, *J. Appl. Phys.* **92**, 4312 (2002).

[27]   H. Ye, G. W. Wicks and P. M. Fauchet, *Appl. Phys. Lett.* **74**, 711 (1999).

Chapter Four: Coherent acoustic phonons in GaN single crystals

Recent advances in femtosecond lasers and ultrafast spectroscopy now allow us to study the coherent phenomena in semiconductors, which are directly related to the microscopic details of the coupling mechanisms. In this chapter, we focus on generation and detection of CAPs in GaN crystals. This macroscopic coherence phenomenon is on a time scale of a hundred femtoseconds to a few tens of picoseconds and results from the nonzero quantum averages of the phonon creation and annihilation operators, in other words, the macroscopic displacements of the lattice. Depending on the particular interaction of the optical excitation with the lattice, both coherent optical and coherent acoustic phonons can be generated, but here, we focus only on CAPs. The difference between the coherent and incoherent acoustic phonons is that only CAPs can cause a macroscopic lattice displacement, while the incoherent phonons give rise of quantum fluctuations of the lattice equilibrium. The CAPs are launched by the ultrafast photoexcitation of nonequilibrium carriers via interband transitions. This electronic perturbation in the microscopic environment is sufficiently fast, to initiate a synchronized motion of many different acoustic phonon modes, whose phases are locked. This collective

motion can propagate in the material as a coherent wavepacket, called the CAP pulse, and modulate the material properties.

On a microscopic level, the dynamics of CAPs is described by the Hamiltonian [1]:

$$\hat{H} = \sum_{a,k} \varepsilon_{ak} c_{ak}^{+} c_{ak} + \sum_{q} \hbar\omega_q b_q^{+} b_q + \sum_{a,k,q} M_{k,q}^{a} (b_q + b_{-q}^{+}) c_{ak}^{+} c_{a,k+q} , \qquad (4.1)$$

where c, c^{+} are the electron second quantization operators in k space, $\varepsilon_{a,k}$ is the energy in band $a = \{c,v\}$ (conduction or valence). The free acoustic phonon Hamiltonian is represented by the second term in Eq. (4.1), where ω_q, b_q^{+} and b_q are the phonon frequency and the phonon creation and annihilation operators. The acoustic phonon dispersion relation is given by a relation $\omega_q = v_s |q|$ where v_s, q are the acoustic phonon sound speed and wave vector. The last term in the Hamiltonian represents the electron-acoustic phonon interaction with $M^a{}_{k,q}$ as the interaction matrix. The phonon operators are related to the lattice displacement operator $\hat{u}$ by the standard expression [1]:

$$\hat{u}(r) = \sum_{q} \sqrt{\frac{\hbar}{2\rho V \omega_q}} \left\{ b_q e^{iq\cdot r} + b_q^{+} e^{-iq\cdot r} \right\} , \qquad (4.2)$$

where ρ is the reduced mass density and V is the system volume.

The coherent phonon amplitude of the qth phonon mode is defined to be [1]:

$$D_q = \langle b_q(t) \rangle + \langle b_{-q}^+(t) \rangle,$$ (4.3)

so that it is proportional to the Fourier components of the displacement:

$$\langle \hat{u}_q \rangle \equiv \left\langle \frac{1}{V} \int d^3 r \hat{u}(r) e^{-iq \cdot r} \right\rangle = \sqrt{\frac{\hbar}{2\rho V \omega_q}} D_q.$$ (4.4)

The equation of motion for the coherent phonon amplitude D_q can be established using an operator form of the Heisenberg equation. Commuting the Hamiltonian (4.1) with the phonon annihilation operator and taking the averages, one gets

$$\frac{\partial \langle b_q \rangle}{\partial t} = i\omega_q \langle b_q \rangle + i\sum_{a,k} M_{kq}^a n_{k,k+q}^a,$$ (4.5)

where, $n_{k,k+q}^a = \langle c_{ak}^+ c_{a,k+q} \rangle$ is the electron density matrix, which depends on the optical excitation conditions. Taking a time derivative and adding Eq. (4.5) for $\langle b_q \rangle$ and $\langle b_{-q}^+ \rangle$, one obtains the equation of motion for the coherent phonon amplitude D_q:

$$\frac{\partial^2}{\partial t^2} D_q + \omega_q^2 D_q = -2\omega_q \sum_{a,k} M_{kq}^a n_{k,k+q}^a \,. \qquad (4.6)$$

Equation (4.6) is a driven harmonic oscillator equation. Since the acoustic phonon dispersion relation is linear, the microscopic harmonic-oscillator [Eq. (4.6) for the coherent phonon amplitude] can be transformed into a loaded-string equation (elastic wave equation with a forcing term) for the lattice displacement field u in the space-time domain. As an example, the one-dimensional loaded-string equation is [2]

$$\frac{\partial^2}{\partial t^2} u(z,t) - v_s^2 \frac{\partial^2}{\partial z^2} u(z,t) = S(z,t), \qquad (4.7)$$

where the driving function $S(z,t)$ is given by

$$S(z,t) = \sum_{a,k,q} \sqrt{\frac{2\hbar v_s |q|}{\rho V}} M_{kq}^a n_{k,k+q}^a \,, \qquad (4.8)$$

which includes the details considered in the microscopic theory. This latter phenomenological model greatly simplifies the mathematical treatment of the generation and propagation of CAPs without losing any essential physics and has been adopted in our work.

CAPs excited by ultrafast laser pulses have been investigated before, using optical pump–probe spectroscopy in GaN thin films, $In_xGa_{1-x}N/GaN$

heterostructures, and multiple quantum wells [2-6]. A common feature of such structures is the existence of a significant lattice mismatch, which results in highly strained interfaces. Since GaN and its alloys are piezoelectric semiconductors with large piezoelectric constants, the presence of strain at the interface gives rise to a strong, of-the-order-of-several-MV/cm [6], built-in piezoelectric field. When a pump laser pulse excites electron-hole pairs, the strain-induced piezoelectric field spatially separates the electrons and holes and, in turn, serves as the source of CAP generation.

In addition to the piezoelectric effect, two other CAP-generation mechanisms have been reported in literature [7,8]: the deformation-potential-coupled electronic stress and the heat-induced thermal stress. Both of these stresses originate in the transient photoexcitation of electron-hole pairs in the material. In one case, the transition of electrons from the valence band to the conduction band breaks the lattice equilibrium and results in a deformation of the lattice. Such deformation, in turn, alters the semiconductor band structure and induces the electronic stress coupled to the conduction-band free carriers through the deformation potential. In the other case, the photoexcited carriers simply transfer their excess energy to the lattice via electron–phonon scattering, as they relax down towards the band edge. The fast cooling process of hot carriers produces a sharp increase of the lattice temperature, leading to the thermal stress.

Among the above-mentioned mechanisms of CAP generation, the piezoelectric effect is always the dominant contribution in the strained systems, studied in Refs. 2-6, while the other two, typically, play only a very weak role, as

discussed in Ref. 6. However, in semiconductor single crystals (GaN, in our case), there is obviously no lattice-mismatch–induced strain and the piezoelectric field cannot be built. Thus, the CAP generation in bulk samples can only be due to either the electronic or thermal stress, or both, depending on the photon excitation energy and the studied material's properties.

In this chapter, I depict our systematic experimental and detailed theoretical modeling studies on the first all-optical generation and detection of CAPs in bulk GaN crystals with the two-color ultraviolet/blue–near-infrared (UV/blue–NIR), time-resolved femtosecond pump–probe technique. Our theoretical modeling follows the seminal work of Thomsen *et al.* [8], is based on the one-dimensional elastic wave equation and diffusion effects, and predicts that the electronic stress is clearly the dominant factor in CAP generation in GaN single crystals. For a CAP detection mechanism, we have derived an analytic expression for the time-dependent, probe-beam reflectivity change caused by the propagating CAPs.

Experimentally, we have utilized UV femtosecond pump pulses to excite the CAPs at the sample surface and detected them by measuring the $\Delta R/R$ signal of a time-delayed NIR probe pulse. We observed the CAP oscillations superimposed on the exponentially decaying $\Delta R/R$ electronic transient, with the amplitude of the order of 10^{-5} to 10^{-6} and frequency linearly dependent (no dispersion) on the probe-beam wave number. We have varied the energy of the pump excitation pulses from far above the GaN bandgap, through near bandgap, up to just below bandgap (band-tail states). In all cases, we were able to easily produce measurable CAP oscillations, and,

by careful investigation of their amplitude changes as a function of the energy (wavelength) of pump photons, we confirmed that indeed the CAPs in GaN existed due to the electronic stress. By using in all of our tests probe beams with photon energies far below the GaN bandgap (corresponding wavelengths were around 800 nm), we took advantage of a very small, ~50-cm^{-1}, absorption coefficient (very weak attenuation) of probe light in GaN crystals [9] and were able to demonstrate that the CAP pulses propagated deeply into the GaN crystal volume without any measurable loss of coherence/attenuation (the CAP oscillations were easily resolved with the pump-probe delay of up to 10 ns, which was the time limit of our experimental setup).

4.1 Theoretical modeling

Extending the approach presented by Thomsen *et al.* [8], we have developed a theoretical model of the generation, propagation, and detection of CAPs in bulk GaN crystals, studied using a femtosecond, two-color pump–probe technique. In our scheme, the laser pump pulse with the photon energy above the material bandgap excites both the electronic and thermal stress at the sample surface. These two stresses act as the driving terms in the elastic wave equation that describes generation and propagation of CAPs. The propagating CAPs modulate optical properties of the GaN dielectric function, which is represented as disturbance of a dielectric permittivity in the Maxwell equations. By solving the Maxwell equations, we

obtained an expression for the time-dependent modulation of the $\Delta R/R$ transient caused by the traveling CAP waves, which, in turn, could be directly measured in our experiments, using below-bandgap probe pulses.

We stress that the Thomsen model was developed to explain generation and detection of CAPs in α–As_2Se_3 bulk samples and semiconductor and metallic thin films, using a picosecond, one-color pump–probe method [8]. In such a case, the CAP generation was assumed to be solely due to the thermal stress and detection was limited in a near-surface region, due to the very strong sample absorption of the probe beam. In our model, we consider both the electronic- and thermal-stress generation mechanisms. Since GaN exhibits relatively large deformation potential and different coefficients in ambipolar and thermal diffusion, the contribution of the electronic stress to the CAPs amplitude and shape is different from that of the thermal stress. Our theoretical calculations show that in GaN, CAPs generated by the electronic stress have actually the strength an order of magnitude larger than that generated by the thermal stress and the two stresses have different pump-photon-energy dependences.

4.1.1. CAP pulse generation

We consider a femtosecond UV pump pulse with photon energy higher than the GaN bandgap that is incident on the surface of a bulk GaN crystal. Given that the diameter of the irradiated area is much larger than the UV pulse absorption depth (the

lateral gradient of the absorbed light power is therefore much smaller the normal one), both the electronic and thermal stress generated by the pump pulse can be assumed to depend only on the z axis, which is defined to be perpendicular to the sample surface and pointing into the sample. Therefore, the lattice displacement has a nonzero component only in the z direction and, in our case, the CAP generation is reduced to a one-dimensional (1-D) problem.

As we have discussed above, the equation of motion for the coherent phonon amplitude is the driven harmonic oscillator equation and for CAPs, because their phonon dispersion relation is linear, this microscopic harmonic-oscillator equation can be transformed into an elastic wave equation with a forcing term, expressed by Eq. (4.7) for the 1-D case. We note that Eq. (4.7) is the equation for the lattice displacement u in the space-time domain. However, it is usually more straightforward and convenient to express the CAP field by the non-zero component of the elastic strain tensor η_{zz}, defined as $\eta_{zz}(z,t) = \partial u(z,t)/\partial z$. Therefore, the 1-D elastic (nondissipative) wave equation for η_{zz}, describing generation and propagation of CAPs, can be written as

$$\frac{\partial^2 \eta_{zz}(z,t)}{\partial t^2} - v_s^2 \frac{\partial^2 \eta_{zz}(z,t)}{\partial z^2} = \frac{\partial}{\partial z} S(z,t). \qquad (4.9)$$

In the Thomsen phenomenological model [8], the driving function $S(z,t)$ can be found to relate to thermal stress $\sigma_{zz}^{th}(z,t) = -3B\beta\Delta T(z,t)$ through $S(z,t) = \frac{1}{\rho}\frac{\partial}{\partial z}\sigma_{zz}^{th}(z,t)$,

where B is the bulk modulus, β is the linear thermal expansion coefficient, and $\Delta T(z,t)$ is the lattice temperature rise. Similarly, in our case, the driving force can be defined as

$$S(z,t) = \frac{1}{\rho}\frac{\partial}{\partial z}(\sigma_{zz}^{th} + \sigma_{zz}^{e}), \qquad (4.10)$$

where σ_{zz}^{e} is the electronic stress, which was not included in the Thomsen treatment. Like σ_{zz}^{th}, σ_{zz}^{e} is also a function of z and time t and can be expressed as

$$\sigma_{zz}^{e}(z,t) = d_c n_e(z,t) - d_v n_h(z,t), \qquad (4.11)$$

where d_c and d_v are the conduction-electron and valence-hole deformation potentials respectively, and, $n_e(z,t)$ and $n_h(z,t)$ are the photoexcited electron and hole densities, respectively. In general, $n_e(z,t)$ and $n_h(z,t)$ have different spatiotemporal evolutions, but, since in our case they are initially excited in equal numbers by the same pump pulse, we are going to ignore their differences and assume that $n_e(z,t) \approx n_h(z,t) = n(z,t)$, and, hence, Eq. (4.11) becomes

$$\sigma_{zz}^{e}(z,t) = \left(d_c - d_v\right)n(z,t). \qquad (4.12)$$

Assuming that both the carrier motion and the heat conduction have a diffusive character, we utilize a simple transport model to describe the evolution of $n(z,t)$ and $\Delta T(z,t)$:

$$\frac{\partial n(z,t)}{\partial t} - D\frac{\partial^2 n(z,t)}{\partial z^2} = 0, \qquad (4.13)$$

$$\frac{\partial \Delta T(z,t)}{\partial t} - \chi\frac{\partial^2 \Delta T(z,t)}{\partial z^2} = 0, \qquad (4.14)$$

with the initial conditions

$$n(z,0) = \frac{\alpha_{\text{pump}}\left(1 - R_{\text{pump}}\right)Q}{E_{\text{pump}}}\exp\left(-\alpha_{\text{pump}}z\right), \qquad (4.15)$$

$$\Delta T(z,0) = \frac{\alpha_{\text{pump}}\left(1 - R_{\text{pump}}\right)Q}{E_{\text{pump}}} \times \frac{E_{\text{pump}} - E_g}{C_V}\exp\left(-\alpha_{\text{pump}}z\right), \qquad (4.16)$$

and boundary conditions

$$D\frac{\partial n(0,t)}{\partial z} = 0, \qquad (4.17)$$

$$\chi \frac{\partial \Delta T(0,t)}{\partial z} = 0, \qquad (4.18)$$

where D is the ambipolar diffusion coefficient of the GaN electron-hole plasma, χ is the thermal diffusivity, R_{pump}, Q, α_{pump}, and E_{pump} are the reflectance, fluence, absorption coefficient, and photon energy of the pump beam, and C_V is the specific heat per unit volume. We have also assumed above that for the duration of our ~150-fs-wide pump pulses, the photoexcitation is instantaneous and the plasma diffusion is negligible.

The solutions for the diffusion equations (4.13) and (4.14) with the initial conditions (4.15), (4.16) and the boundary conditions (4.17), (4.18) are

$$n(z,t) = \frac{1}{2} \frac{(1-R_{pump})Q}{\xi_{pump}AE_{pump}} e^{(-z+Dt/\xi_{pump})/\xi_{pump}} \times$$
$$\left[2 - \mathrm{Erfc}\left(\frac{z-2Dt/\xi_{pump}}{\sqrt{4Dt}} \right) + e^{2z/\xi_{pump}} \mathrm{Erfc}\left(\frac{z+2Dt/\xi_{pump}}{\sqrt{4Dt}} \right) \right] \qquad (4.19)$$

and

$$\Delta T(z,t) = \frac{1}{2} \frac{(1-R_{pump})Q}{\xi_{pump}AE_{pump}} \frac{E_{pump}-E_g}{C_V} e^{(-z+\chi t/\xi_{pump})/\xi_{pump}} \times$$
$$\left[2 - \mathrm{Erfc}\left(\frac{z-2\chi t/\xi_{pump}}{\sqrt{4\chi t}} \right) + e^{2z/\xi_{pump}} \mathrm{Erfc}\left(\frac{z+2\chi t/\xi_{pump}}{\sqrt{4\chi t}} \right) \right], \qquad (4.20)$$

where Erfc(x) is the complementary error function.

Knowing the $n(z,t)$ and $\Delta T(z,t)$ distributions, we can numerically solve the wave Eq. (4.9), subject to the initial, $t = 0$, and elastic boundary, $z = 0$, conditions:

$$\eta_{zz}(z,0) = 0, \qquad\qquad\qquad (4.21)$$

$$\eta_{zz}(0,t) = \frac{1}{\rho V_s^2}\left[3B\beta\Delta T(0,t) - \left(d_c - d_v\right)n(0,t)\right]. \quad (4.22)$$

In our analysis of the CAP generation, the two trigger mechanisms, namely, the electronic and thermal stress, are completely decoupled. Thus, the CAP fields excited by each mechanism can be treated separately and the total CAP field is just the simple sum of both the electronic and thermal components. Figure 4.1 presents examples of numerically computed profiles of CAP transients, generated by electronic stress, thermal stress, and the sum of both, respectively. The CAP pulses plotted in Fig. 4.1(a) were calculated for the far-above-bandgap pump-photon excitation (photon energy of 4.59 eV; corresponding wavelength 270 nm), while those shown in Fig. 4.1(b) correspond to the excitation using just-above-bandgap pump photons (energy of 3.54 eV; wavelength 350 nm). In both cases, Q was kept constant and equal to 0.08 mJ/cm^2/pulse, the value actually implemented in our pump–probe experiments, while the α_{pump} values were taken to be 2.07×10^5 cm^{-1} and 1.29×10^5 cm^{-1}, corresponding to the pump photon energies of 4.59 eV and 3.54

eV, respectively [9]. The other GaN material parameters used in our calculations can be found in Table 4.1.

As we see in Fig. 4.1, the CAP pulses have strength of the order of 10^{-5} and a spatial width of approximately twice the pump beam penetration depth $\left(\varsigma_{pump} = 1/\alpha_{pump}\right)$. We note that our simulations predict that in GaN the electronic stress contribution is the major, dominant factor in the CAP generation, as compared to the thermal-stress contribution, in both the far-above- and just-above-bandgap excitations [Figs. 4.1(a) and 4.1(b), respectively], with the strength ratio between the electronic- and thermal-induced CAPs equal to about 8 and 60 for the 4.59- and 3.54-eV pump photons, respectively. Electronically induced strength of CAPs decreases only slightly when the pump photon energy decreases from 4.59 eV to 3.54 eV, while the thermal one drops by about an order of magnitude. Thus, the change of the total CAP strength is small [see Figs. 4.1(a) and 4.1(b), bottom curves], as it is electronic-stress dominated. The CAP amplitude is mainly determined by α_{pump}, which changes only a little in the studied, above-bandgap, pump energy region.

The shapes of all CAP pulses presented in Fig. 4.1 are asymmetrically bipolar with a slight broadening at their trailing sides. This broadening is caused by the diffusion effects [8] and is much more pronounced in the electronic-induced CAPs because the electron-hole diffusion is about 5 times faster than the thermal diffusion. The diffusion effects not only broaden the CAP pulse, but they also narrow its frequency spectrum, as is shown in the inset in Fig. 4.1 (a), where the spectra of the electronic- and thermal-induced CAPs are compared.
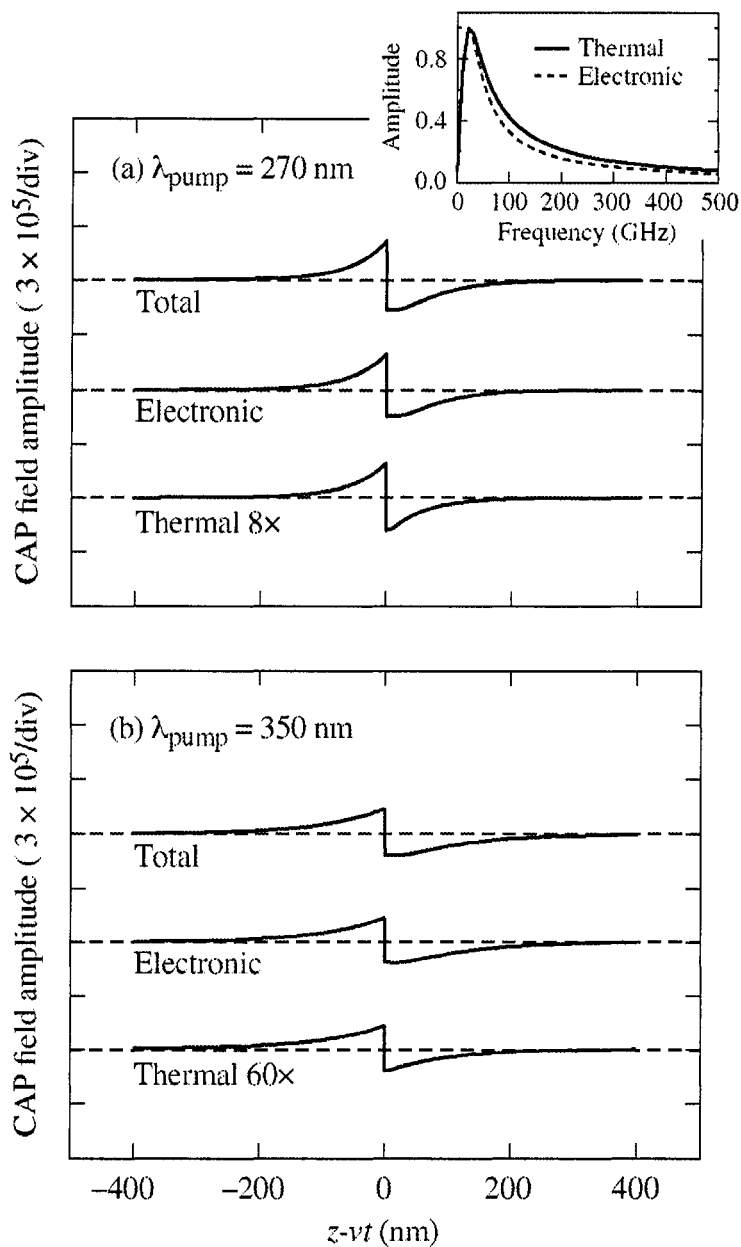
FIG. 4.1. Simulation of spatial-time profiles of propagating CAP transients generated by the electronic stress, thermal stress, and both, respectively. The CAP pulses shown in (a) and (b) were excited by the pump photons with a photon energy of 4.59 eV and 3.54 eV (wavelengths 270 nm and 350 nm), respectively. The inset shows the frequency spectra of the electronically (solid line) and thermally induced (dashed line) CAP.

Table 4.1. Material parameters for wurtzite GaN.

Parameter	GaN
Longitudinal sound velocity v_s (m/s)	8020[a]
Mass density ρ (g/cm^3)	6.15[b]
Bulk modulus B (GPa)	207[c]
Linear thermal expansion coefficient β (K^{-1})	3.17×10^{-6} [d]
Electron deformation potential d_c (eV)	-4.08[e]
Hole deformation potential $d_v =$ D1 + D3 (eV)	2.1[f]
Ambipolar diffusion coefficient D (cm^2/s)	2.1[g]
Thermal diffusivity χ (cm^2 s^{-1})	0.43[b]
Band gap E_g (eV)	3.4[h]
Specific heat per unit volume C_V (J cm^{-3}°C^{-1})	3.01[b]

[a]C. Deger *et al.*, Appl. Phys. Lett. **72**, 2400 (1998).

[b]V. Bougrov *et al.*, in *Properties of Advanced Semiconductor Materials: GaN, AlN, InN, BN, SiC, SiGe*, edited by M. E. Levinshtein, S. L. Rumyantsev, and M. Shur (Wiley, New York, 2001), Chap. 1, p. 1.

[c]M. Leszczynski *et al.*, J. Phys. D: Appl. Phys. **28**, A149 (1995).

[d]W. Qian, M. Skowronski, and G. S. Rohrer, in *III-Nitride, SiC, and Diamond Materials for Electronic Devices*, edited by D. K. Gaskill, C. D. Brandt, and R. J. Nemanich, Mat. Res. Soc. Symp. Proc. Vol. 423 (Materials Research Society, Pittsburgh, PA, 1996), p. 475.

[e]S. L. Chuang and C. S. Chang, Phys. Rev. B **54**, 2491 (1996).

[f]G. D. Sanders and C. J. Stanton, Phys. Rev. B **64**, 235316 (2001).

[g]G. Tamulaitis *et al.*, Phys. Status Solidi C **3**, 1923 (2006).

[h]S. N. Nakamura and G. Fasol, *The Blue Laser Diode: GaN Based Light Emitters and Lasers* (Springer, Berlin, 1997).

4.1.2. CAP pulse detection

In the discussed GaN sample geometry, the surface-generated CAP pulses propagate into the crystal along z-axis, causing a spatiotemporal modulation of the material's dielectric function. This modulation can be detected through the change in the reflectivity R of a time-delayed probe beam. The detection scheme is schematically shown in Fig. 4.2. The NIR probe beam is incident on the sample and generates two reflection beams. One is partially reflected from the sample's surface and the other is directly reflected from the CAP pulse. The interference between these two reflection beams produces the single-frequency oscillations on top of the experimentally observed probe's $\Delta R/R$ signals.

We stress that the frequency of the interference-caused oscillations corresponds to the only one CAP mode. As we have discussed at the beginning of this chapter, many different CAP modes are instantaneously launched by the ultrafast photoexcitation of nonequilibrium carriers. These CAPs are bunched together into a broadband CAP pulse [Fig. 4.1] with a bandwidth of several hundred GHz. The interaction of the probe photons with the CAP pulse follows the momentum selection rule [10]: $q = k_i + k_f \approx 2nk_0$, where q is the wave vector of one CAP mode, k_i and k_f are the initial and final wave vectors of the probe beam, n is the real part of the refractive index, and k_0 is the probe beam wave vector in air. Thus, the scattering process provides a "probe filter"—the probe photons scatter exclusively on the single wave-vector-matched CAP mode.

Taking into account the linear dispersion relation of the CAPs in the near-zone-center region: $q = 2\pi f/v_s$, the frequency f of the CAP mode with the wave vector q can be related to the probe beam through $f = \dfrac{nv_s}{\pi}k_0$. Therefore, by changing the probe beam wavelength, different CAP modes can be "selected" and experimentally measured.
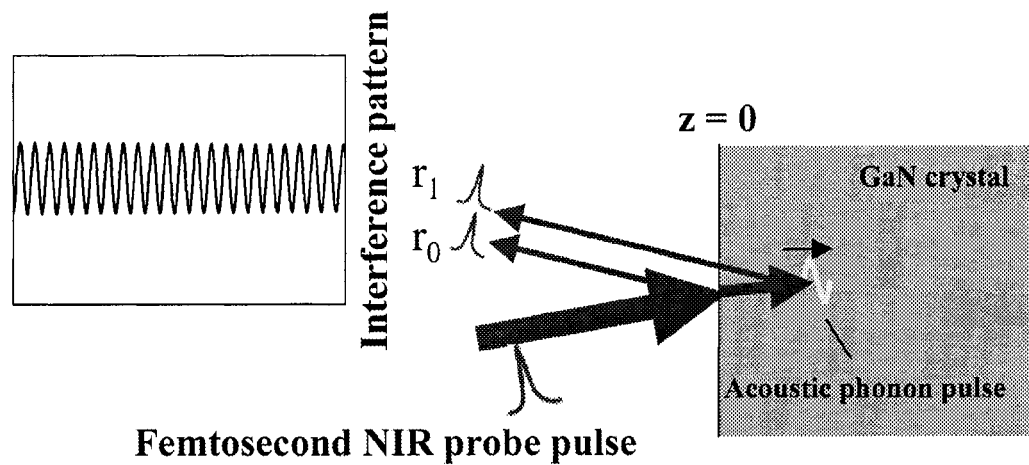
Fig. 4.2. CAP pulse detection scheme by using a NIR probe beam.

In the presence of the CAP pulse, the probe beam $\Delta R/R$ can be expressed as

$$\Delta R / R = \frac{\left|r_0 + \Delta r\right|^2 - \left|r_0\right|^2}{\left|r_0\right|^2}, \qquad (4.23)$$

where r_0 is the reflection coefficient at the sample surface and represents that part of the probe beam electric field reflected from the free surface, while Δr corresponds to the probe electric field reflected from the CAP pulse. In the case of normal incidence, r_0 is expressed by

$$r_0 = \frac{1 - \tilde{n}}{1 + \tilde{n}} = \frac{1 - n - i\kappa}{1 + n + i\kappa}, \qquad (4.24)$$

where $\tilde{n} = n + i\kappa$ is the complex refractive index and κ is the imaginary part of the refractive index. We note that κ is related to the probe-beam absorption coefficient α_{probe} or, equivalently, the penetration depth ζ_{probe} through $\kappa = \alpha_{\text{probe}}\lambda/4\pi = \lambda/4\pi\zeta_{\text{probe}}$, where λ is the probe-beam wavelength.

The CAP pulse induced Δr can be obtained by solving the Maxwell equations inside the GaN sample with the presence of the CAP-pulse-caused disturbance of the dielectric function:

$$\frac{\partial^2 E(z,t)}{\partial z^2} + \frac{\omega^2}{c^2}[\varepsilon + \Delta\varepsilon(z,t)]E(z,t) = 0, \quad (4.25)$$

where $E(z,t)$ is the electric field of the probe light, ω, c are the angular frequency of the probe light and the light speed in vacuum, respectively. ε is the dielectric constant in GaN in the absence of the CAP pulse, and is related to n and κ through $\varepsilon = \tilde{n}^2 = (n + i\kappa)^2$. $\Delta\varepsilon(z,t)$ is the change in ε, which, under assumption that the disturbance is caused only by the propagating CAP pulse, can be written as

$$\Delta\varepsilon(z,t) = 2(n + i\kappa)\left(\frac{dn}{d\eta_{zz}} + i\frac{d\kappa}{d\eta_{zz}}\right)\eta_{zz}(z,t). \quad (4.26)$$

Equation (4.25) is the inhomogeneous Helmholtz equation and can be solved using the standard Green's function theory. The Green's function is determined by solving

$$\frac{\partial^2 G(z,z')}{\partial z^2} + \frac{\omega^2}{c^2}\tilde{n}^2 G(z,z') = \delta(z - z') \quad (4.27)$$

and the result is

$$G(z,z') = -\frac{i}{2\tilde{n}k_0}\exp(i\tilde{n}k_0|z - z'|). \quad (4.28)$$

Then, the solution to Eq. (4.25) can be written as

$$E(z,t) = E_h(z,t) + \int_{-\infty}^{\infty} dz' G(z,z')[-k_0^2 \Delta \varepsilon(z',t) E_h(z',t)], \quad (4.29)$$

where $E_h(z,t)$ is the homogeneous solution, which describes the probe light

propagating in the sample in the absence of the CAP pulse and takes the form

$$E_h(z,t) = t_0 E_0 \exp[i(\tilde{n} k_0 z - \omega t)], \quad (4.30)$$

where $t_0 = \dfrac{2}{1+\tilde{n}} = \dfrac{2}{1+n+ik}$ is the transmission coefficient of the probe beam from

air into the sample at normal incidence and E_0 is in $E_i(z,t) = E_0 \exp[i(k_0 z - \omega t)]$,

where $E_i(z,t)$ is the electric field of the incident probe beam. The integral in Eq. (4.29)

represents the electric field disturbance caused by the CAP pulse. If we consider only

the part of the probe-beam electric field reflected from the CAP pulse, the integral

becomes

$$\int_0^{\infty} dz' (-\frac{i}{2\tilde{n} k_0}) e^{i\tilde{n} k_0 (z'-z)} [-k_0^2 \Delta \varepsilon(z',t) E_h(z',t)]$$

$$\equiv \left[\frac{ik_0}{2\tilde{n}} \int_0^{\infty} dz' e^{2i\tilde{n} k_0 z'} \Delta \varepsilon(z',t) \right] t_0 E_0 \exp[-i(\tilde{n} k_0 z + \omega t)]. \quad (4.31)$$

This probe beam reflected from the CAP pulse will then partially cross the sample-air interface and, hence, the total reflected probe-beam electric field in the presence of the CAP pulse becomes:

$$E_r(z,t) = \left\{ r_0 + \tilde{t}_0 t_0 \left[\frac{ik_0}{2\tilde{n}} \int_0^\infty dz' e^{2i\tilde{n}k_0 z'} \Delta\varepsilon(z',t) \right] \right\} E_0 e^{-i(k_0 z - \omega t)}, \qquad (4.32)$$

where $\tilde{t}_0 = \dfrac{2\tilde{n}}{1+\tilde{n}} = \dfrac{2(n+i\kappa)}{1+n+i\kappa}$ is the transmission coefficient of the probe beam from the sample into air. From Eq. (4.32), Δr can be finally determined as

$$\Delta r = \tilde{t}_0 t_0 \left[\frac{ik_0}{2\tilde{n}} \int_0^\infty dz' e^{2i\tilde{n}k_0 z'} \Delta\varepsilon(z',t) \right]$$

$$= \frac{4i\omega(n+i\kappa)}{c(1+n+i\kappa)^2} \int_0^\infty \left[\frac{\partial n}{\partial \eta_{zz}} + i\frac{\partial \kappa}{\partial \eta_{zz}} \right] \eta_{zz}(z,t) e^{2i(n+i\kappa)k_0 z} dz. \quad (4.33)$$

Knowing r_0 and Δr, the probe's $\Delta R/R$ can be readily calculated through Eq. (4.23). However, the analytic expression of $\Delta R/R$ can be obtained only if the $\eta_{zz}(z,t)$ functional dependence is known. Unfortunately, we have $\eta_{zz}(z,t)$ only in a numerical form presented in Fig. (4.1), but we can approximate it by a simple analytic expression:

$$\eta_{zz}(z,t) = -Ae^{-\alpha_{pump}|z-v_s t|}\,\text{sgn}(z-v_s t), \qquad (4.34)$$

which fits our numerical stress pulses very well and only neglects the electron-hole and thermal diffusion effects in the CAP generation. A is the strength of the CAP pulse given by

$$A = \frac{\alpha_{pump}(1-R_{pump})Q}{2E_{pump}\rho v_s^2}\left[-(d_c+d_v)+\frac{3B\beta}{C_V}(E_{pump}-E_g)\right]. \qquad (4.35)$$

Combining the above formulas and considering that for our two-color pump–probe technique the condition $\alpha_{pump} \gg \alpha_{probe}$ holds, we find an analytical expression for $\Delta\varepsilon(z,t)$ and, finally, we obtain the main result: the closed-form formula for $\Delta R/R$, correct to the first order in $\eta_{zz}(z,t)$:

$$\Delta R/R = \sqrt{\left(\frac{dn}{d\eta_{zz}}\right)^2+\left(\frac{d\kappa}{d\eta_{zz}}\right)^2}\,AF_1\left[\sin\left(\frac{4\pi n v_s t}{\lambda}-\phi\right)e^{-v_s t/\zeta_{probe}}+F_2 e^{-v_s t/\zeta_{pump}}\right], (4.36)$$

where

$$F_1 = \frac{8\sqrt{n^2(n^2+\kappa^2-1)^2+\kappa^2(n^2+\kappa^2+1)^2}}{n(n^2+\kappa^2+1)^2-4n^3} \qquad (4.37)$$

is the probe-beam–related amplitude,

$$\phi = \arctan\left[\frac{\kappa(\mathrm{n}^2 + \kappa^2 + 1)}{n(\mathrm{n}^2 + \kappa^2 - 1)}\right] + \arctan\left[\frac{dn/d\eta_{zz}}{d\kappa/d\eta_{zz}}\right] \qquad (4.38)$$

is the phase, and

$$F_2 = \frac{8\pi^2 n^2 \sin\phi - 2\pi n\lambda\alpha_{\mathrm{pump}}\cos\phi}{16\pi^2 n^2 + \lambda^2\alpha_{\mathrm{pump}}^2}. \qquad (4.39)$$

Equation (4.36) allows us to directly compare our theoretical modeling with the experiments, facilitating data analysis and making our results more explicit. We can, however, further simplify Eq. (4.36) by noting that under our experimental conditions, ζ_{pump} is of the order of several tens of nanometers; thus, for the GaN sound speed $v_s = 8020$ m/s [11], the second term in the square bracket in Eq. (4.36) rapidly damps out within several picoseconds and it can be neglected, as in our experiments we study CAPs within at least a few-hundred-ps-wide time delay window. The expression (4.36) with the second term in the square bracket omitted reads as

$$\Delta R/R = \sqrt{\left(\frac{dn}{d\eta_{zz}}\right)^2 + \left(\frac{d\kappa}{d\eta_{zz}}\right)^2}\, AF_1 \sin\left(\frac{4\pi n v_s t}{\lambda} - \phi\right) e^{-v_s t/\zeta_{\mathrm{probe}}}. \qquad (4.40)$$

The temporal dependence of $\Delta R/R$ is represented in Eq. (4.40) as a simple damped-sinusoidal function and it follows Eq. (48) in Ref. 8, but now we have also an expression for the $\Delta R/R$ amplitude, as the product of A, F_1, and $\sqrt{\left(dn/d\eta_{zz}\right)^2 + \left(d\kappa/d\eta_{zz}\right)^2}$. The probe-related F_1 [see Eq. (4.37)] can be considered as a constant since for far-below-bandgap, NIR light, n and κ in high-quality GaN crystals remain almost unchanged. The $dn/d\eta_{zz}$ and $d\kappa/d\eta_{zz}$ terms are the photoelastic constants and they are related only to n and κ, thus, $\sqrt{\left(dn/d\eta_{zz}\right)^2 + \left(d\kappa/d\eta_{zz}\right)^2}$ also contributes a constant term in the total $\Delta R/R$ amplitude. Finally, following Eq. (4.35), the term A (strength of the CAP pulse) is only pump light related. We note that A experiences a dramatic change when the pump energy is tuned across the band edge because of the step-like change of α_{pump} near E_g. Experimentally it means that the total $\Delta R/R$ amplitude measured using the two-color pump–probe technique should change with the pump-beam energy, following the same functional dependence as A, namely the spectral characteristics of α_{pump}. Furthermore, this theoretical prediction indicates that we should be able to undeniably determine which stress contribution—electronic or thermal—is the dominant factor for triggering the CAPs in our bulk GaN crystals. If the electronic stress is dominant, as we have predicted in Sec. 4.1.1, the experimentally observed $\Delta R/R$ amplitude should exhibit only a slight decrease when the pump energy changes

from far-above to just-above bandgap. On the other hand, when the thermal stress is dominant, the oscillation amplitude should experience an-order-of-magnitude drop in the same pump energy range. Independently, when the pump beam energy is tuned across band edge, the amplitude of the experimental $\Delta R/R$ signal should almost abruptly decease to zero, due to the rapid decrease of α_{pump}.

In agreement with the Thomsen model [8], the $\Delta R/R$ damping constant in Eq. (4.40) is determined by the ζ_{probe}/v_s ratio. For ~800-nm wavelength probe light used in our two-color measurements ζ_{probe} is ~200 μm for GaN [9], which gives the damping time $\zeta_{probe}/v_s \approx 25\,\text{ns}$. Thus, we should observe CAPs propagating deeply into the GaN crystal, actually, in full agreement with our experimental studies.

Following again Eq. (4.40), the frequency of the $\Delta R/R$ oscillations is given by

$$f = 2nv_s/\lambda = \frac{nv_s}{\pi}k_0 \qquad (4.41)$$

and is related only to the probe beam. For a constant n, expected under our experimental conditions, f is proportional to k_0, which indicates a linear dispersion relation for CAPs with the slope corresponding to the fixed v_s. Finally, ϕ [see Eq. (4.38)] is, in our experimental case, predicted to be a constant.

4.2. Experimental procedures and results

Two-color, femtosecond pump–probe spectroscopy experiments were performed in a reflection mode at room temperature. The experimental setup has been described in Chap. 2. In our study of CAPs in GaN single crystals, two arrangements were used to generate the pump beam with desired photon energy (see Fig. 2.9). One optical path was designed to deliver photons with energies in the range of 3.1 to 3.54 eV (wavelength: 400 to 350 nm) in the vicinity of the GaN bandgap of 3.4 eV and was based on frequency doubling of the fundamental Ti:sapphire pulse train. The other included the third-harmonic generator and allowed us to generate pump photons with energies ranging from 4.38 eV to 4.71 eV (wavelength from 283 nm to 263 nm), far above the GaN bandgap. The pump beam, after passing through a UV-pass filter, was focused onto the surface of the GaN crystal with a spot diameter of ~20 μm at an incident angle of ~30°. The incident fluence was ~0.08 mJ/cm^2 per pulse and was kept constant while varying the pump photon energy. Probe pulses had photon energies varying from 1.46 eV to 1.77 eV (wavelengths from 850 nm to 700 nm) far below the GaN gap; their fluence was always much lower (at least by a factor of 10) than that of the pump. The probe beam was normally incident on the sample surface with a spot diameter ~10 μm. We have studied CAP oscillations by varying the energy of the pump excitation pulses from far above the GaN bandgap, through near bandgap, up to just below bandgap (band-tail states). We added fixed optical delays between the pump and probe beams in order to investigate CAP oscillations at long

time delays up to 10 ns. The magnitude of the probe $\Delta R/R$ that we measured was in the range of 10^{-3} to 10^{-6}.

Typical time-resolved $\Delta R/R$ signals from our GaN crystal excited with far-above-bandgap (wavelength of 283 nm) and just-above-bandgap (wavelength of 350 nm) pump photons are shown in Figs. 4.3(a) and 4.3(b), respectively. The corresponding probe wavelengths were 850 nm in Fig. 4.3(a) and 700 nm in Fig. 4.3(b). As we can see, although the two presented $\Delta R/R$ waveforms exhibit different electronic relaxation features, observed during the initial few picoseconds of relaxation and associated with the conduction band inter- and intra-valley electron scattering (see Chap. 3), both are characterized by the same, few-hundred-ps-long exponential decay, associated with the electron-hole recombination, with pronounced regular oscillations on top of it.
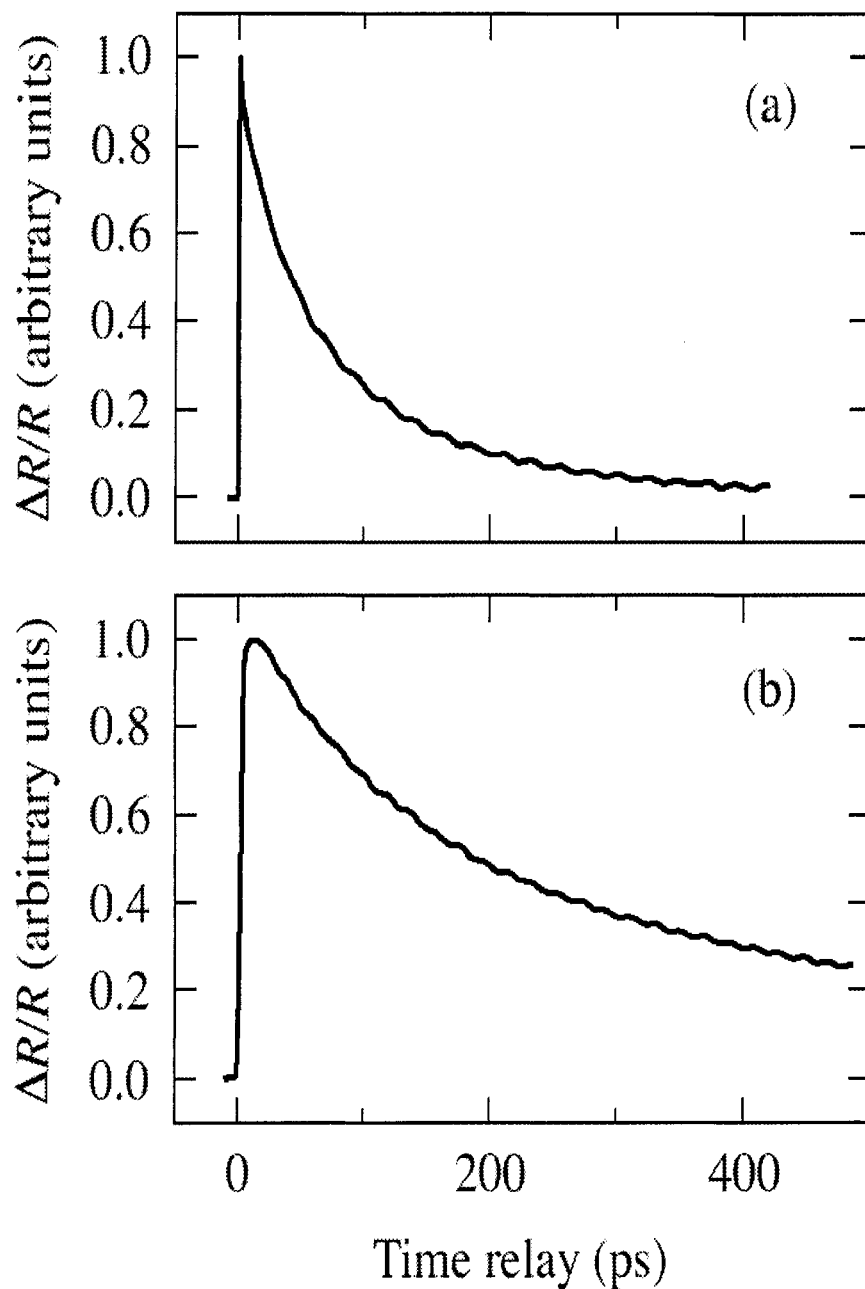
FIG. 4.3. Time-resolved normalized $\Delta R/R$ waveforms as a function of the pump-probe delay time, measured in GaN single crystals for (a) the pump/probe wavelength of 283 nm/850 nm; (b) pump/probe wavelength of 350 nm/700 nm. The case (a) corresponds to the far-above-bandgap optical excitation, while case (b) to just-above-bandgap excitation.

Here, obviously, we focus only on this latter oscillatory feature, which we identify as propagation of the CAP transient inside the crystal. Thus, in order to get a clearer view, we have numerically subtracted the electronic relaxation background from all our collected raw data. Figure 4.4(a) shows the oscillatory component of the measured $\Delta R/R$ signal for four experimental examples, representative of our measurement cases. The presented traces correspond to the three different experimental conditions for CAP excitation, namely, far-above-bandgap excitation (trace 283 nm/850 nm), just-above-bandgap excitation (traces 350 nm/700 nm and 360 nm/720 nm), and band-tail-state excitation (trace 370 nm/740 nm), respectively. In all cases, no attenuation of the oscillations is observed within our experimental ~450-ps-wide time-delay window, which is consistent with our theoretical prediction that the CAP oscillation damping constant is limited by the $\zeta_{\mathrm{probe}}/v_s$ ratio and under our experimental conditions $\zeta_{\mathrm{probe}}/v_s \approx 25 \, \mathrm{ns}$, which is much longer than our experimental time window.

Figure 4.4(b) presents four $\Delta R/R$ CAP-related transients calculated using Eq. (4.40) and corresponding directly to the four experimental transients shown in Fig. 4.4(a). In our theoretical calculations, $n = 2.3$ and the probe $\alpha_{\mathrm{probe}} = 50 \, \mathrm{cm}^{-1}$ are assumed to remain unchanged for all the studied probe wavelengths. The pump reflectance R_{pump} was set to be 0.2 and the constants $d n/d\eta_{zz}$ and $d\kappa/d\eta_{zz}$ entering into Eqs. (4.38) and (4.40) were set to be 1.2 and 0.5, respectively, in order to keep the CAP amplitude and phase consistent with our experimental values. We note that

there is extremely good agreement between the corresponding experimental [Fig. 4.4(a)] and theoretical [Fig. 4.4(b)] traces, in terms of both the oscillation amplitude and frequency.
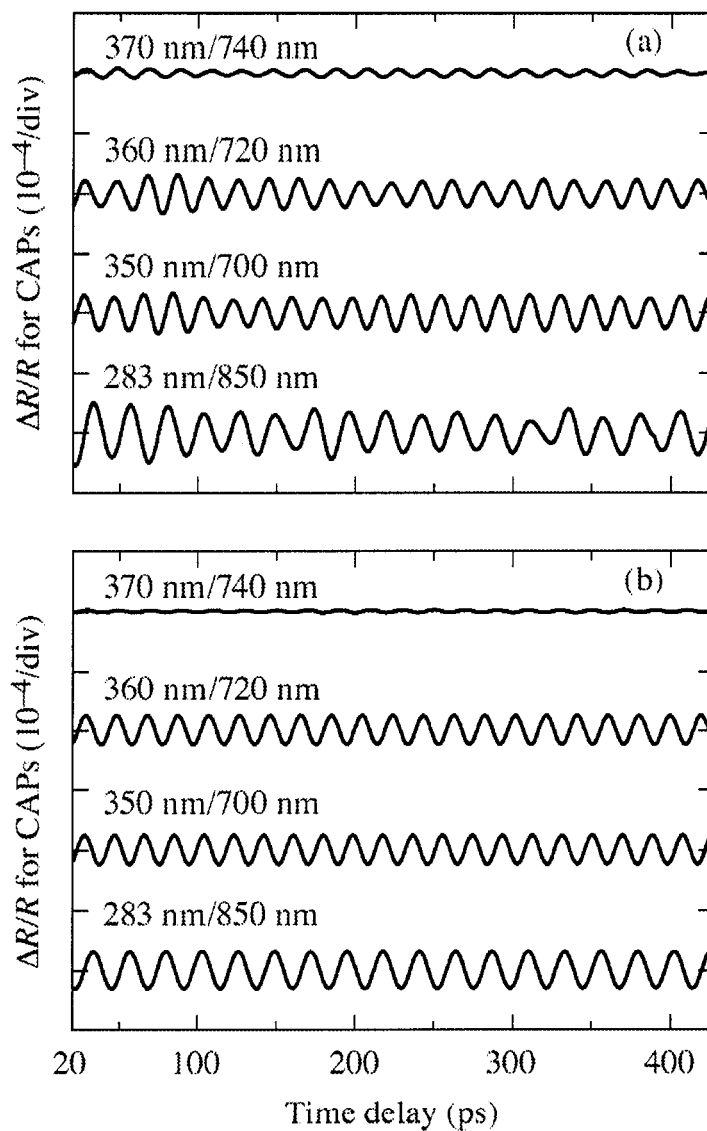

Fig. 4.4. The oscillatory components of $\Delta R/R$ signals as a function of the pump-probe delay time for several pump/probe wavelength configurations: 370 nm/740 nm, 360 nm/720 nm, 350 nm/700 nm, and 283 nm/850 nm. Panels (a) and (b) show the experimental and theoretical results, respectively.

Comparing the traces 283 nm/850 nm, 350 nm/700 nm, and 360 nm/720 nm, we observe only a slight amplitude decrease as we move from the far-above- to just-above-bandgap excitation. On the other hand, the 370-nm/740-nm trace, collected for the pump photon energy corresponding to GaN band-tail states, has a much smaller amplitude than the other three, but the oscillatory feature is still observable. The above findings experimentally confirm our theoretical prediction that the driving mechanism for CAP generation in bulk GaN crystals is the electronic stress associated with the deformation potential.

The rapid drop in the CAP amplitude that occurs when we move the energy of our excitation photons across the GaN bandgap (compare traces 360 nm/720 nm and 370 nm/740 nm in Fig. 4.4) is caused by the dramatic change of the α_{pump} coefficient at the band edge. The latter is clearly illustrated in Fig. 4.5, where we plot the CAP oscillation amplitude dependence on the pump-photon wavelength (energy) for the whole pump tuning range. The solid line shows the theoretical $\Delta R/R$ amplitude dependence on the pump-photon energy, based on Eq. (4.40) [see also Eq. (4.35)]. We used the values listed in Ref. 9 for the α_{pump} spectral dependence in GaN crystals. The solid squares, circles, and triangles represent our experimental data corresponding to the far-above-bandgap, just-above-bandgap, and band-tail-state pump excitations, respectively. We see very good overall agreement between our experimental points and the modeling. Only in the case of the pump photons exciting the band-tail states (solid triangles in Fig. 4.5), the decrease of the CAP amplitude with the pump-wavelength increase is slower than our theoretical prediction. The

latter discrepancy, however, is clearly a consequence that in our calculations we used the values of α_{pump} from Ref. 9 and not α_{pump} directly measured for our GaN samples. The dashed line in Fig. 4.5 corresponds to the GaN absorption coefficient spectrum extracted from the transmission and reflection data of our actual GaN sample, experimentally measured using a Perkin-Elmer Lambda 900 spectrophotometer. We note that in this case the agreement is excellent.
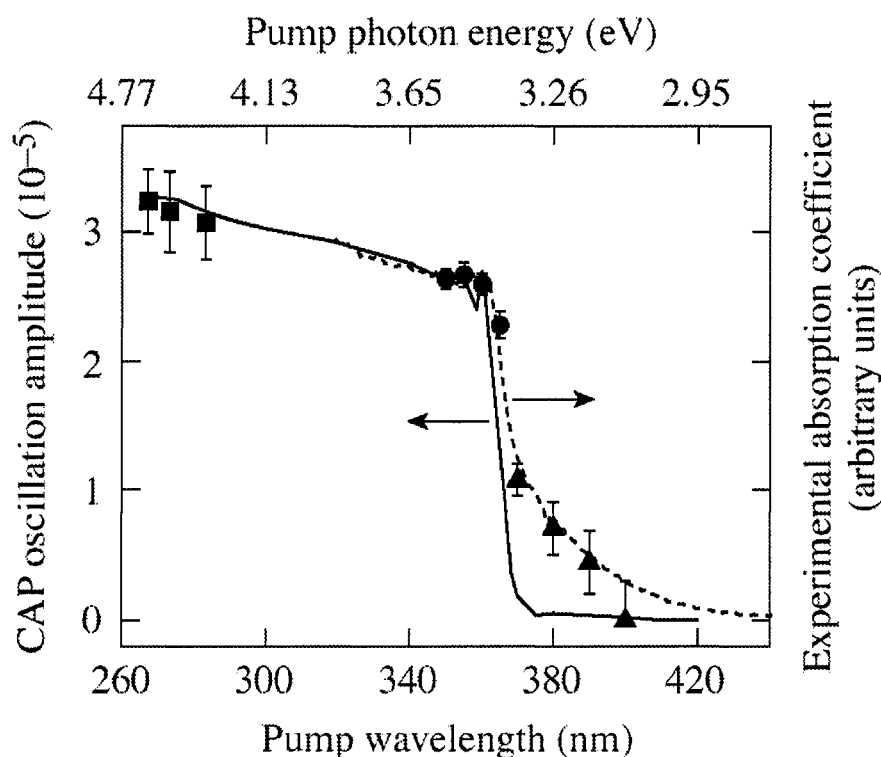
Fig. 4.5. The amplitude of the CAP oscillations versus the pump beam wavelength (energy–top axis). The solid line is the theoretical curve, while the solid squares, circles, and triangles are our experimental data points corresponding to the far-above-bandgap, just-above-bandgap, and band-tail-state pump excitations, respectively. The dashed line (right axis) is the experimental GaN absorption coefficient spectrum, extracted from the transmission and reflection data obtained for our actual GaN single crystal.

For all the traces plotted in Fig. 4.4, the CAP oscillation phase was essentially constant and equal to ~1.2, as is shown in Fig. 4.6, which presents ϕ as a function of the probe photon wavelength (energy) for our entire experimental tuning range. The constant ϕ is very consistent with our theoretical prediction based on Eq. (4.38) and the fact that n, κ, $dn/d\eta_{zz}$ and $d\kappa/d\eta_{zz}$ can be assumed constant for our NIR probe photons. The solid line in Fig. 4.6 was obtained by fitting Eq. (4.38) with $(dn/d\eta_{zz})/(d\kappa/d\eta_{zz}) = 2.5$ as the best fit.
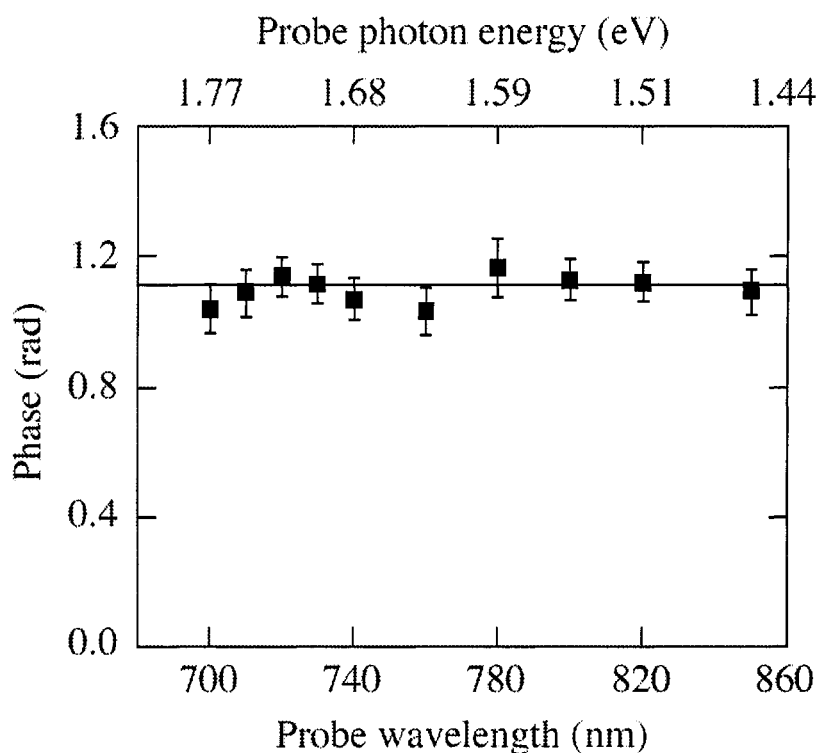
Fig. 4.6. The phase of the CAP oscillation versus the probe beam wavelength (energy–top axis). The solid line shows the theoretical fit based on Eq. (4.38) with $\dfrac{dn/d\eta_{zz}}{d\kappa/d\eta_{zz}} = 2.5$.

The dispersion relation of the CAP oscillation frequency on the probe beam wave number was investigated as well, as shown in Fig. 4.7. For the entire probe-beam tuning range from 700 nm to 850 nm, we observe a linear (dispersionless) relationship between f and k_0, as predicted by Eq. (4.41). The slope of the data (solid line in Fig. 4.7) gives v_s = 8002±22 m/s. The latter result is very close to 8160-m/s and 8020-m/s values reported in literature [3,11].
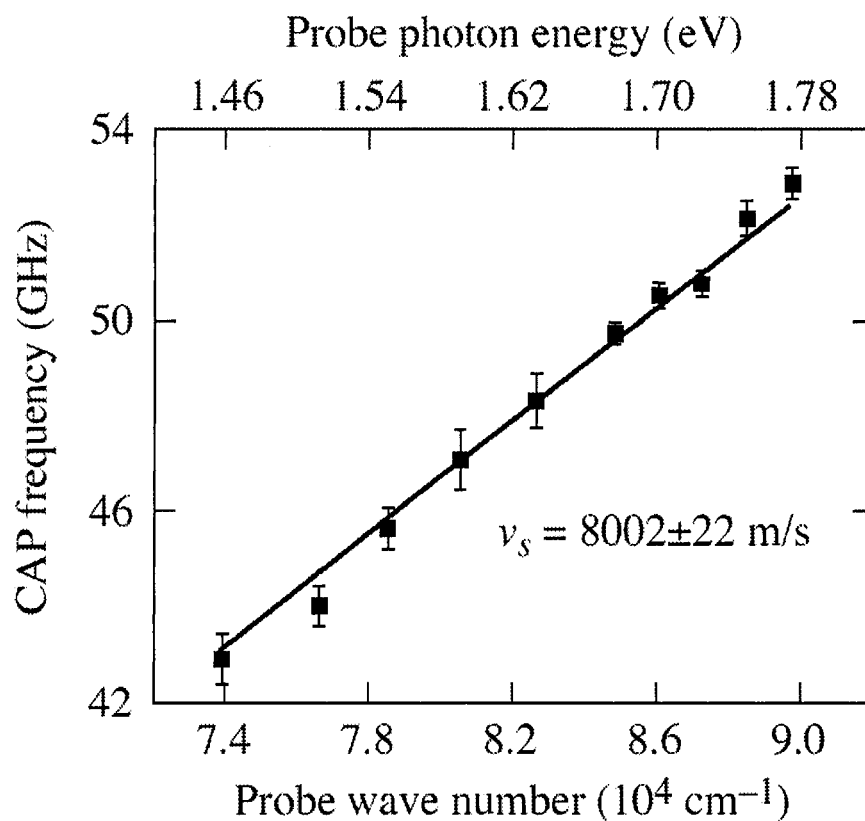

Fig. 4.7. CAP oscillation frequency dependence on the probe beam wave number (energy–top axis). The solid squares are the peak values of the CAP oscillations Fourier spectra, while the solid line shows the linear fit, intercepting the plot origin, based on Eq. (4.41).

Finally, we attempted to measure or, at least, estimate the intrinsic attenuation of CAP oscillations. The time-delay window in Fig. 4.4 is only 450 ps, limited by the extent of our delay line, and we do not see any attenuation of the CAP signal. In order to study our CAP oscillations at longer delays, we added fixed optical delays between the pump and probe beams so that the translational delay stage could scan individual, 150-ps time windows starting from 1 ns, 2.5 ns, and 10 ns. We note that the 10-ns delay is practically the longest achievable delay time for our measurement setup because of the 76-MHz repetition rate (pulse separation of 13.2 ns) of our Ti:sapphire laser.

Figure 4.8 shows the CAP oscillations measured at the above-mentioned time windows with a pump and probe wavelengths of 267 nm and 800 nm, respectively. While we see damping of the $\Delta R/R$ signal as the delay time increases, the oscillation period remains the same for all cases. Compared to other published reports where the CAP oscillations were usually completely damped out within several tens or hundreds of picoseconds [3,4,8,12], our observations report the longest lifetime of coherent acoustic oscillations in solids, as they clearly remain alive within the entire 10-ns time range of our experiment. From Eq. (4.40), we know that the attenuation of CAP oscillation is determined by the finite probe beam penetration depth in GaN, however, an assumption that the intrinsic CAP attenuation is negligible is placed there. If we consider both the probe beam and the intrinsic CAP attenuations, the experimental damping time constant τ_d of the CAP oscillations can be expressed as a simple superposition:

$$\frac{1}{\tau_d} = \frac{1}{\tau_{phonon}} + \frac{1}{\varsigma_{probe}/v_s}, \qquad (4.42)$$

where τ_{phonon} is the intrinsic CAP lifetime. The solid lines in Fig. (4.8), representing theoretical fits based on Eq. (4.40), yielded $\tau_d = 19.2\pm0.4$ ns at $\lambda_{probe} = 800$ nm. Giving that $\varsigma_{probe} \approx 200$ μm at 800 nm and the sound speed $v \approx 8002$ m/s in GaN, $\varsigma_{probe}/v_s \approx 25$ ns. Therefore, our experimental τ_d is limited by the finite penetration depth of the probe light. CAPs in our GaN crystals are actually very long-lived and the intrinsic τ_{phonon} estimated using Eq. (4.42) is ~ 83 ns at room temperature.
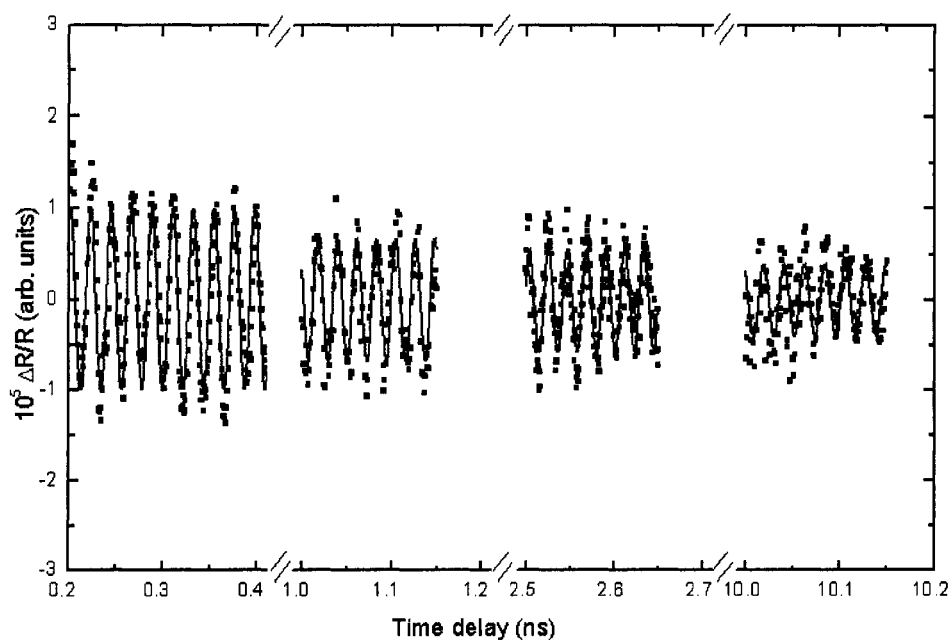
Fig. 4.8. CAP oscillations (black squares) in different time-delay windows: 0.2 ns — 0.35 ns, 1 ns — 1.15 ns, 2.5 ns — 2.65 ns, and 10 ns — 10.15 ns, measured at a pump wavelength of 267 nm and a probe wavelength of 800 nm. Solid lines are the theoretical fits, based on Eq. (4.40) with a single frequency f = 45 GHz and the damping time constant τ_d = 19.2 ns.

4.3. Conclusions

In this chapter, we have presented our comprehensive studies of CAP generation and detection in the bulk GaN single crystals, using a time-resolved, femtosecond, two-color pump–probe technique. We theoretically predicted and experimentally confirmed that the CAP transients, in our case, were initiated by the electronic stress induced at the GaN crystal surface by generation of free carriers, photoexcited by ~150-fs pump UV pulses. Using far-below-bandgap, ~100-fs-wide probe pulses with a very long penetration depth into the GaN crystal, we monitored the CAP propagation that manifested itself as regular, single-frequency oscillations superimposed on the probe $\Delta R/R$ signal. The amplitude of the oscillations was of the order of 10^{-5} to 10^{-6}. Within our 10 ns time delay window, we observed oscillation attenuation which was simply due to the probe beam absorption in GaN and implied the intrinsic CAP lifetime is much, much longer. We also found that the CAP oscillation amplitude was dependent only on the pump photon energy and, in general, followed the spectral dependence of the GaN optical absorption coefficient, as was predicted by our theoretical model. For the entire tuning range of our NIR probe photons, the phase of the CAP oscillations was constant and the CAP frequency was dispersionless (proportional to the probe k_0) with the slope corresponding to $v_s = 8002\pm22$ m/s, the speed of sound in GaN. The very good agreement between our theoretical modeling and experimental results demonstrates that our theoretical approach, which is a generalization of the Thomsen model [8], comprehensively

describes the dynamics of CAPs in bulk materials, generated by the strong, above-the-bandgap optical excitation and synchronously probed using almost non-attenuated probe pulses. Thus, our above-bandgap pump and far-below-bandgap probe experimental approach makes it possible to successfully generate nanoscale acoustic waves at the surface of bulk semiconductors and, simultaneously, to nondestructively probe the material's structure deeply under its surface. The two-color femtosecond spectroscopy technique, implemented here for the studies of GaN, should be very promising in producing and detecting CAP waves in a large variety of bulk semiconducting materials and multi-layer structures.

References:

[1]   A. V. Kuznetsov and C. J. Stanton, *Phys. Rev. Lett.* **73**, 3243 (1994).

[2]   R. Liu, G. D. Sanders, C. J. Stanton, C. S. Kim, J. S. Yahng, Y. D. Jho, K. J. Yee, E. Oh and D. S. Kim, *Phys. Rev. B* **72**, 195335 (2005).

[3]   Y.-K. Huang, G.-W. Chern and C.-K. Sun, *Appl. Phys. Lett.* **79**, 3361 (2001).

[4]   C.-K. Sun, J.-C. Liang and X.-Y. Yu, *Phys. Rev. Lett.* **84**, 179 (2000).

[5]   Ü. Özgür, C.-W. Lee and H. O. Everitt, *Phys. Status Solidi B* **228**, 85 (2001).

[6]   G. D. Sanders and C. J. Stanton, *Phys. Rev. B* **64**, 235316 (2001).

[7]   O. Matsuda, T. Tachizaki, T. Fukui, J. J. Baumberg and O. B. Wright, *Phys. Rev. B* **71**, 115330 (2005).

[8]   C. Thomsen, H. T. Grahn, H. J. Maris and J. Tauc, *Phys. Rev. B* **34**, 4129 (1986).

[9]   G. Yu,   G. Wang, H. Ishikawa, M. Umeno, T. Soga, T. Egawa, J. Watanabe and T. Jimbo, *Appl. Phys. Lett.* **70**, 3209 (1997).

[10]   I. Bozovic, M. Schneider, Y. Xu, R. Sobolewski, Y. H. Ren, G. Lüpke, J. Demsar, A. J. Taylor and M. Onellion, *Phys. Rev. B* **69**, 132503 (2004).

[11]   C. Deger, E. Born, H. Angerer, O. Ambacher, M. Stutzmann,   J. Hornsteiner, E. Riha and G. Fischerauer, *Appl. Phys. Lett.* **72**, 2400 (1998).

[12]   O. Matsuda, O. B. Wright, D. H. Hurley, V. E. Gusev and K. Shimizu, *Phys. Rev. Lett.* **93**, 095501 (2004).

Chapter Five: Conclusions

5.1 Thesis summary

Ultrafast carrier and phonon dynamics in semiconductors have been an extremely active field of research and have led to many new insights into phenomena of fundamental importance in the semiconductor physics and technology. In this thesis, we have focused our studies to the following two topics: (1) intervalley transitions of hot electrons, and (2) coherent acoustic phonons, both studies were performed in very high quality GaN single crystals, the most attractive "blue electronics" semiconductor. Although we dealt with two totally different physical processes, our experimental approach was the same: two-color (UV–NIR), time-resolved femtosecond pump–probe technique. This two-color configuration has a distinct advantage over other pump-probe configurations—the far-below-bandgap probe is not sensitive to the details of the studied material's band-gap structure nor to any interband absorption, making results of pump-probe studies easy to interpret.

In such UV-NIR pump-probe experiments, a typical time-resolved, probe-beam $\Delta R/R$ signal, as shown in Fig. 5.1, demonstrates three different features: the initial, few-ps-wide, fast decay of the $\Delta R/R$ transient, identified as the intervalley electronic transition process of photoexcited carriers in GaN; relatively slow, few-hundred-ps-long exponential decay associated with the electron-hole recombination; and finally, the pronounced regular oscillations that are superimposed on top of the

electron-hole recombination background and correspond to propagation of CAP

transients inside the GaN crystal.
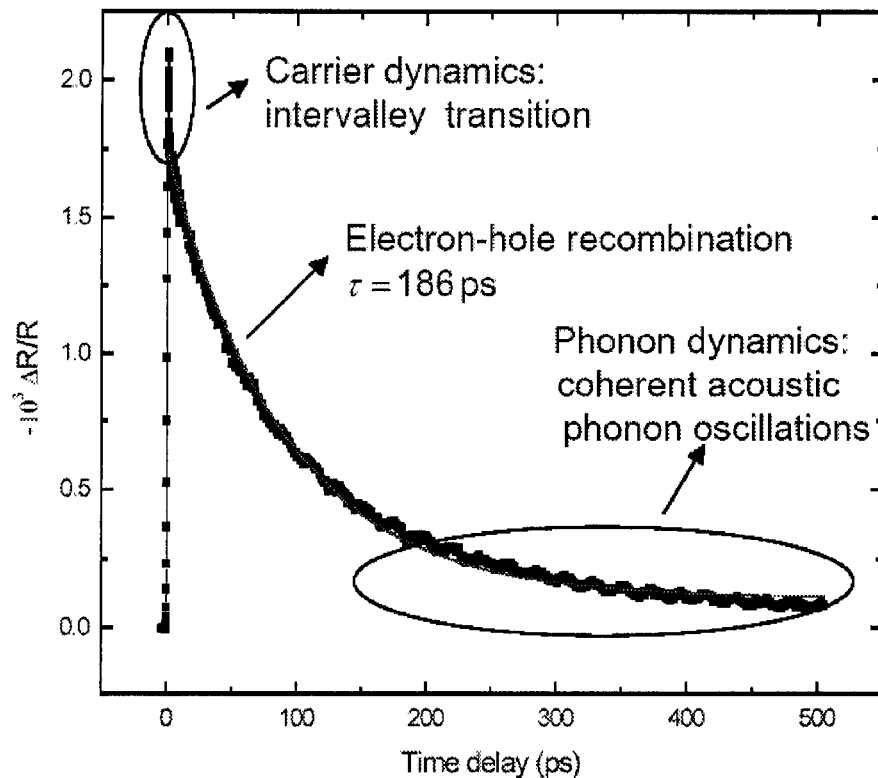
Fig. 5.1. Typical time-resolved normalized reflectivity change ΔR/R signal from our GaN crystal excited with the pump wavelength of 267 nm and probed with the wavelength of 801 nm. Solid line represents the best-exponential-fit corresponding to electron-hole recombination.

The intervalley transitions were addressed in Chap. 3. There, we have

presented the detailed experimental and theoretical studies of intervalley scattering of

hot electrons in high-quality bulk GaN crystals. We directly observed the time-

resolved electron population change in the Γ and L valleys with our two-color, pump–

probe configuration at both the room temperature and 100 K, and determined that the energy threshold for the $\Gamma \leftrightarrow L$ transition was 4.51 eV at room temperature and 4.57 eV at 100 K. We have also numerically solved the three-state rate equations governing the intervalley scattering dynamics. The solutions fitted extremely well our experimental data. From the fits, we determined the characteristic scattering time constants, defining the dynamics of both the intervalley and intravalley transitions. Finally, we estimated the intervalley deformation potential in GaN and found it in a good agreement with the value reported in literature.

In Chap. 4, we have presented our very comprehensive and systematic theoretical and experimental studies of the CAP oscillation properties in GaN bulk crystals from every possible aspect, including amplitude, phase, frequency, as well as attenuation. Our theoretical approach is a generalized Thomsen model. In the generation process of CAPs, we derived the CAP field induced by electronic stress, thermal stress, and both, respectively. We have found that the electronic-stress- and the thermal-stress-generated CAP fields had different characteristics in terms of the field strength dependence on the pump photon energy, and we predicted that the electronic stress was the main trigger for CAP generation.

In modeling of the detection of CAPs, our emphasis was focused on how the amplitude, phase, frequency, as well as damping of the CAP oscillations, depended on the energies of pump and probe photons. In our far-below-bandgap detection scheme, we derived a closed-form analytical expression for the transient reflectivity change caused by the propagating CAP pulse. We demonstrated that the amplitude of

the CAP oscillations was determined by the pump pulse energy (actually the absorption coefficient of pump photons), while their phase was nearly a constant.

In the experimental part, we did extensive experimental studies of CAPs generated using far-above-bandgap, just-above-bandgap, and just-below-bandgap (band-tail states) pump photons. The studies allowed us to obtain a detailed dependence of the CAP oscillations amplitude on the pump-photon energy/wavelength, as well as unambiguously conclude that the electronic stress (and NOT thermal stress) was the CAP trigger in our bulk GaN crystals, excited by femtosecond optical pulses. In addition, we presented the dependence of the phase of the CAP oscillations on the probe beam wavelength/energy. Finally, our experimental CAP dispersion relation (f vs. k_0) extended over a wide range of probe beam wave vectors. The actual dispersionless character of the f vs. k_0 curve allowed us to very precisely determine the speed of sound in GaN.

5.2 Future work

5.2.1 Study of intrinsic CAP lifetime in GaN single crystals

It is of great interest to determine the intrinsic CAP lifetime in our GaN crystals. We have studied the attenuation of CAP oscillations in Chap. 4 and attributed the observed damping of the oscillations to the finite penetration depth of the probe light within the longest achievable delay times for our measurements. However, our experimental configuration did not allow us to detect the CAP pulse

propagating beyond the probe light penetration depth, making the direct measurement of the actual intrinsic CAP lifetime impossible.

Here, we propose a modified one-color UV pump-probe experimental geometry, as shown in Fig. 5.2. We use femtosecond UV laser pulses to excite the front surface of the GaN crystal and generate the CAP transients at the surface region. As the CAP pulses propagate toward the other side of the GaN sample, they are subjected to the attenuation because our GaN sample is thick. Once they reach the surface on the far side of the sample, they can be detectable by means of the change in probe beam reflectivity induced at the back surface. Time-delayed optical probe pulses with the same wavelength as the pump pulses (to measure CAPs only at the surface), provide the time-resolved measurement of the CAP oscillations. By calculating the ratio of the amplitudes of the CAP oscillations individually measured at each side of the sample and taking into account the probe beam attenuation, the intrinsic CAP pulse lifetime can be quantitatively determined as shown in Eq. (4.42).
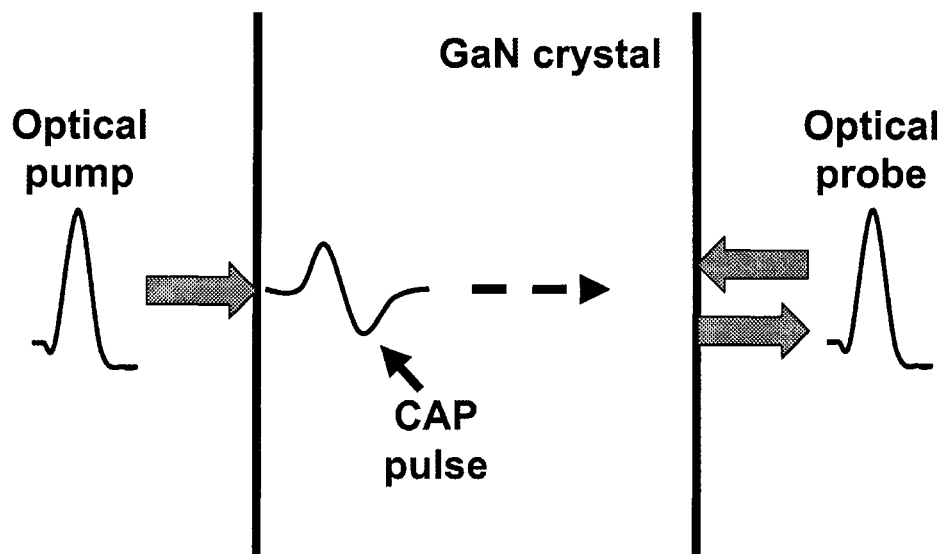
Fig. 5.2. Schematic diagram of one-color UV pump-probe experiment.
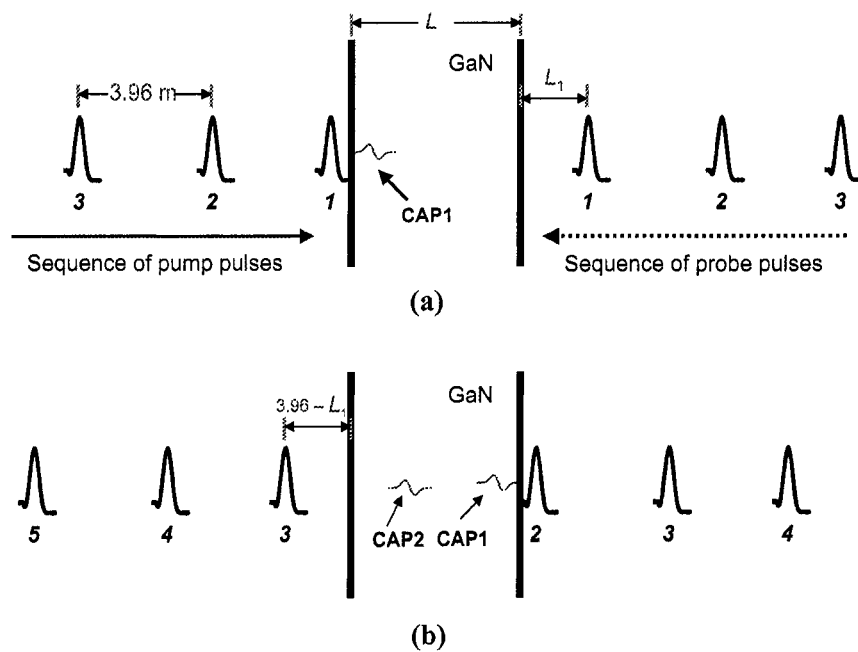

(a)

(b)

Fig. 5.3 CAP pulse detection strategy.

In order to detect the CAP pulse at the far-side surface of our sample, a practical problem arises how to obtain a long enough time delay between the pump and probe pulses. For the sample thickness of 0.4 mm, it requires time of ~50 ns for the CAP pulse to travel from one side of the sample to the other, which means that the probe beam has to be delayed by at least 50 ns with respect to the pump in order to encounter the CAP pulse at the far-side surface. Converting to the space domain, the optical delay for the probe beam has to be set as ~15 meters. Such a long distance makes the maintenance of a precise alignment of the optical beam over the entire delay extremely difficult. In addition, we need to remember that the pulse separation in our laser is only 13.2 ns.

In order to solve this problem, we propose to follow the approach presented in Ref. 1, where the length of the delay line can be adjusted from zero up to that of the laser cavity so that arbitrary delays can be realized. Our strategy is schematically shown in Fig. 5.3. There are two points that we want to stress here:

(1)   the probe pulse, when arriving at the far-side sample surface, must encounter a CAP pulse;

(2)   this CAP pulse does not have to be the one excited by the same cycle pump pulse.

In Fig. 5.3, pump and probe pulses labeled with the same number originate from the same laser pulse, and the label "CAP1" (or "CAP2") means that the given CAP pulse was generated by the pump pulse 1 (or 2). Two successive pulses have a distance separation of 3.96 meters, obtained by multiplying the laser pulse repetition time with

the light speed in vacuum. The distance L in Fig. 5.3 is the sample thickness and L_1 represents the length of an extra delay line that we set in the probe beam path. In our case, the CAP1 pulse generated by the pump pulse 1 is detected by the probe pulse 2, and therefore the relationship between L_1 and L can be expressed as

$$\frac{L_1}{c} = \frac{L}{v_s} - 13.2 \times 10^{-9}. \qquad (5.1)$$

Since c and v_s are known and L can be measured, L_1 can be determined. For a generalized case, where the CAP pulse is generated by the pump pulse M and detected by the probe pulse $M+N$, Eq. (5.1) has a form:

$$\frac{L_1}{c} = \frac{L}{v_s} - 13.2 \times 10^{-9} N , \qquad (5.2)$$

where N is an integer. We note that this detection scheme will not be affected by the jitter of the laser because the jitter of our femtosecond Ti:sapphire laser is ~ 1 ps, much shorter than the temporal duration of our CAP pulse (~25 ps).

It would also be very interesting to study the intrinsic CAPs lifetime at cryogenic temperatures. Under such condition, the phonon-phonon scattering should be significantly suppressed and the attenuation of the phonon pulse is expected to be even weaker than at 300 K, allowing phonon propagation over distances of a few millimeters and results in coherence times on the order of microseconds.

5.2.2 Nano-scale photoacoustic microscopy

With rapid advances in nanotechnologies, high-resolution microscopy for non-invasive characterization of subsurface nanostructures becomes a critical challenge. Nowadays, for nanostructure microscopy we are restricted to surface measurements. For non-destructive subsurface imaging, scanning acoustic microscopy is a nature chosen alternative. In this technique, reviewed in Ref. 2 and 3, ultrasound is generated by a piezoelectric transducer focused with a spherical lens. The lens and sample are both immersed in a coupling medium, typically water. The lens is rastered across the sample to be studied and variations in the intensity of reflected acoustic waves are used to form images. Ultrasound is sensitive to the presence of subsurface interfaces and defects; these interfaces and defects appear as regions of bright contrast in the image due to the large acoustic impedance mismatch between the surrounding layer materials and air.

One of the main limitations of conventional acoustic microscopy is that the coupling medium attenuates the ultrasound significantly at high frequencies. While acoustic microscopy has been demonstrated up to 1 GHz for surface imaging, for investigations of interfaces and defects buried deep inside solids, the practical upper limit is typically 150–250 MHz, due to the long focal length of acoustic lenses needed for inspection. In addition to the problem of acoustic attenuation in the coupling medium, complications arise due to the velocity mismatch in the different media, i.e., the velocity mismatch between the lens, water, and the sample under inspection. These changes in the velocity lead to additional aberrations that degrade the

resolution in both the axial and lateral directions and, typically, limit the spatial resolution to several micrometers, while imaging buried layers. Furthermore, the fact that the samples have to be immersed in water often makes them unsuitable for further processing.

We propose a novel microscopy technique for probing buried interfaces that overcomes the above problems by generating and detecting ultrahigh frequency acoustic waves directly using femtosecond laser pulses.

This technique, following the approach presented in Ref. 4, is a non-contact, non-destructive method to probe buried interfaces, it does not require immersion in a coupling fluid, and is based on generation of nanoscale acoustic phonon waves in bulk materials. Our studies have shown the femtosecond laser pulse can excite nanoscale acoustic phonon pulse that travels from the surface into the bulk of a sample. Wherever the CAP signal encounters a discontinuity in the acoustic impedance, a fraction of the phonon transient should be reflected back towards the surface. By using another femtosecond probe pulse to monitor the time and strength of the phonon echoes, information about the axial (z-directional) structure of the examined sample can be obtained. On the other hand, for a transverse scan (in x-y plane), the sample can be placed on a piezostage. By moving the stage, we can perform axial scans point by point in the x-y plane and obtain the reconstructed 2-D or even 3-D images. The axial resolution of the image is essentially determined by the pulse width of the CAP pulse, while the transverse resolution is determined by the scan step in the x-y plane. Since we use femtosecond pulses to excite CAPs, the

phonon pulse has a nanoscale dimension, and, since, the piezostage can provide a nanometer resolution of x-y movements, the proposed microscopy can be achieved with the resolution on the order of a few tens of nanometers. Our study has also shown such CAP pulses have a penetration capability of >100 μm at room temperature, which means that sub-millimeter observation depths can be obtained. Such capability opens up new possibilities of a high-resolution defect and failure detection in semiconductor materials and devices, and should aid in research and development on both evolutionary and disruptive technologies.

References:

[1]   B. C. Daly, T. B. Norris, J. Chen and J. B. Khurgin, *Phys. Rev. B* **70**, 214307 (2004).

[2]   G. A. D. Briggs, *"An Introduction to Scanning Acoustic Microscopy"*, Oxford University Press, Oxford, UK (1985).

[3]   J. Attal, N. T. Quang, G. Cambon, and J. M. Saurel: "Acoustic microscopy: Recent progress in imaging through opaque materials" in *Proceedings of the 2nd Oxford Conference, Microscopy of Semiconducting Materials*, edited by A. G. Cullis and D. C. Joy (IOP, Bristol, UK, 1981), p. 441.

[4]   K. H. Lin, C. T. Yu, S. Z. Sun, H. P. Chen, C. C. Pan, J. I. Chyi, S. W. Huang, P. C. Li and C. K. Sun, *Appl. Phys. Lett.* **89**, 043106 (2006).